

Performance Analysis and Low-Complexity Design for XL-MIMO with Near-Field Spatial Non-Stationarities

Kangda Zhi, Cunhua Pan, Hong Ren, Kok Keong Chai, Cheng-Xiang Wang, *Fellow, IEEE*, Robert Schober, *Fellow, IEEE*, Xiaohu You, *Fellow, IEEE*

Abstract—Extremely large-scale multiple-input multiple-output (XL-MIMO) is capable of supporting extremely high system capacities with large numbers of users. In this work, we build a framework for the analysis and low-complexity design of XL-MIMO in the near field with spatial non-stationarities. Specifically, we first analyze the theoretical performance of discrete-aperture XL-MIMO using an electromagnetic (EM) channel model based on the near-field spherical wavefront. We analytically reveal the impact of the discrete aperture and polarization mismatch on the received power. We also complement the classical Fraunhofer distance based on the considered EM channel model. Our analytical results indicate that a limited part of the XL-array receives the majority of the signal power in the near field, which leads to a notion of visibility region (VR) of a user. Thus, we propose a VR detection algorithm and leverage the acquired VR information to devise a low-complexity symbol detection scheme. Furthermore, we propose a graph theory-based user partition algorithm, relying on the VR overlap ratio between different users. Partial zero-forcing (PZF) is utilized to eliminate only the interference from users allocated to the same group, which further reduces computational complexity in matrix inversion. Numerical results confirm the correctness of the analytical results and the effectiveness of the proposed algorithms. It reveals that our algorithms approach the performance of conventional whole array (WA)-based designs but with much lower complexity.

Index Terms—Extremely-large-scale MIMO, electromagnetic

Part of this work has been accepted by the EUSIPCO, Helsinki, Finland, Sept. 4-8, 2023 [1]. (*Corresponding author: Cunhua Pan.*)

The work of Cunhua Pan was supported in part by the National Natural Science Foundation of China (Grant No. 62201137,62331023). The work of Cunhua Pan and Hong Ren was supported in part by the Fundamental Research Funds for the Central Universities, 2242022k60001, and by the Research Fund of National Mobile Communications Research Laboratory, Southeast University (No.2023A03). The work of H. Ren was supported in part by the National Natural Science Foundation of China (Grant No. 62101128), and in part by Basic Research Project of Jiangsu Provincial Department of Science and Technology (Grant No. BK20210205). The work of Kangda Zhi was supported by China Scholarship Council. The work of C.-X. Wang was supported by the National Natural Science Foundation of China (NSFC) under Grant 61960206006, the Fundamental Research Funds for the Central Universities under Grant 2242022k60006, the Key Technologies R&D Program of Jiangsu (Prospective and Key Technologies for Industry) under Grants BE2022067 and BE2022067-1, and the EU H2020 RISE TESTBED2 project under Grant 872172.

K. Zhi and K. K. Chai are with the School of Electronic Engineering and Computer Science at Queen Mary University of London, UK. (e-mail: k.zhi, michael.chai@qmul.ac.uk).

C. Pan, H. Ren, C.-X. Wang, and X. You are with the National Mobile Communications Research Laboratory, Southeast University, China. (cpan, hren, chxwang, xhyu@seu.edu.cn).

R. Schober is with the Institute for Digital Communications, Friedrich-Alexander-University Erlangen-Nürnberg (FAU), Germany (e-mail: robert.schober@fau.de).

channel model, visibility region, spatial non-stationarities, near-field communications.

I. INTRODUCTION

To fulfill the various challenging demands on the fifth-generation (5G) and beyond wireless systems, several appealing technologies have been proposed and investigated, including massive multiple-input multiple-output (MIMO) [2]–[5], cell-free [6], small cell [7], millimeter-wave (mmWave) [8], and reconfigurable intelligent surface (RIS) [9]–[12]. Among them, as the evolution of massive MIMO, extremely large-scale MIMO (XL-MIMO) has recently garnered new interest [13], [14]. By mounting several thousands of antennas, XL-MIMO can achieve extremely high spectral efficiency and fulfill the harsh data rate requirements of future wireless systems. XL-MIMO may have large physical dimensions spanning several tens of meters [15]. It is expected to be integrated into large structures such as the walls of buildings in megacity, airports, large shopping malls, and stadiums, enabling simultaneous service to a significant number of users.

A classic criterion for distinguishing the boundary between the near and far fields is the Fraunhofer (Rayleigh) distance $d_f = \frac{2D^2}{\lambda}$, where D and λ denote the largest array aperture and wavelength, respectively [16]. As D increases, boundary d_f expands, and the users will be easily located in the near field of the XL-MIMO instead of the far field. Accordingly, the practical spherical electromagnetic (EM) wavefront can no longer be approximated as planar wavefront. There are several distinctions between near-field and far-field communications. The first one is the nonlinear variation of the phase of the received signal across the whole array. Under the far-field condition, the phase of the array steering vector is approximately linearly scaled for different elements, which makes mathematical analysis tractable. However, this characteristic does not hold in the near field. Secondly, as the array aperture increases, it is essential to consider the amplitude/power variation across the entire array. This is because the distance between the user and the array center could be significantly different from that between the user and the array edge. Thirdly, in the near field, the incident wave directions received by distinct antenna elements within the array may exhibit considerable disparities, resulting in substantially varying projected apertures across the whole array. Therefore, for studying XL-MIMO, it is crucial to consider the practical spherical wavefront and investigate the new features introduced by near-field communications.

Taking into consideration the near-field behavior with respect to the whole array, XL-MIMO has recently been studied from different perspectives. Focusing on the nonlinear phases of the array steering vector, some work has investigated beam training [17]–[19], channel estimation [20], and multiple-access design [21]. To further accurately model the near-field spherical wavefront, the variation of the amplitude across the array was considered in [22]–[29]. Specifically, the authors of [22] modeled the near-field channel accounting for the variations of the amplitude and incident wave direction across the whole array. Derived from Maxwell’s equations, the authors of [23]–[25] adopted an EM channel model and characterized the EM polarization effect, which accurately depicts the physical near-field behavior. These works proved that due to the amplitude attenuation at the array edge, despite the aperture of the array approaching infinity, the received power of the signal remains limited. However, for tractability, the above contributions [22]–[29] have assumed the array to be spatially continuous, i.e., edge-to-edge antenna deployment with zero antenna spacing or infinitely large numbers of infinitesimal antennas. This configuration enhances the performance but also causes high fabrication complexity and complicated inter-antenna coupling. By contrast, discrete-aperture XL-MIMO with half-wavelength spacing was studied in [30]–[33]. However, these works did not adopt the EM channel model and therefore the impact of polarization mismatch could not be analyzed.

Another crucial attribute of XL-MIMO is the spatial non-stationarity [15]. Due to the large array dimension, different parts of the array might have different views of the propagation environment. Besides, due to the variations of channel amplitudes and incident wave directions across the whole array, the power of the signal transmitted by a user may be received mainly by a portion of the array, which motivates the notion of user visibility region (VR). The existence of spatial non-stationarities was validated by experimental measurements in [34]. The authors of [35] proposed a near-field channel estimation algorithm for XL-MIMO, which also estimates the mapping between VRs and users. The system performance in the presence of VRs was analyzed in [36]–[39]. By exploiting the feature that users at different locations may possess different VRs, novel algorithms were proposed, in terms of low-complexity detectors [40], random access and user scheduling [38], [41], [42], and antenna selection [43]. Nevertheless, significant research gaps remain. Firstly, most of the existing contributions assumed that the VR information was available for algorithm design. A rigorous VR detection algorithm has not been reported yet. Secondly, for tractability, the uniform linear array (ULA) model was widely adopted in these works. For the general uniform planar array (UPA) model, VR detection and the overlapping relationship between VRs of different users are more complex and challenging. Finally, most of the existing works assumed that the antennas outside the VR do not receive any signal. In practice, these antennas receive small but not zero power, which complicates algorithm design.

To fill the above research gaps, this work investigates discrete-aperture XL-MIMO based on an EM channel model.

We first analyze the impact of the near-field channel on the theoretical performance, which sheds light on the effect of spatial non-stationarities and motivates the design of a VR detection algorithm. Based on the obtained VR information, two low-complexity symbol detection algorithms for XL-MIMO are proposed. The main contributions of this paper are listed as follows.

- Based on the EM channel model, we derive an explicit expression of the signal-to-noise-ratio (SNR) for discrete-aperture XL-MIMO with a single user. We analytically study the near-field characteristics of the SNR, and provide insights into the impact of the discrete aperture and polarization mismatch. We also complement the classical Fraunhofer distance to encompass the impact of arbitrary signal incident directions and the power variations across the whole array in the near field.
- For multi-user XL-MIMO systems, conventional whole array (WA)-based symbol detectors are proposed and analyzed, including maximum ratio combining (MRC), zero-forcing (ZF), and minimum mean-squared error (MMSE) detection. Next, inspired by the insights drawn from the single-user scenario, we propose a sub-arrays-based VR detection algorithm based on the explicit expressions of the received signal power. Then, a VR-based low-complexity linear symbol detection algorithm is proposed.
- To further exploit the VR information and to reduce complexity, we propose a graph theory-based user partition algorithm. The users whose VRs overlap exceeds a certain threshold are partitioned into one group. Then, the partial ZF (PZF) detector is utilized to eliminate only the interference within the group.
- Simulation results are provided to validate the correctness of analytical results and reveal that the proposed algorithms achieve very similar performance as the conventional WA-based design but with much reduced complexity.

The remainder of this paper is organized as follows. Section II provides the EM channel model for near-field wireless systems. Section III derives the closed-form SNR expression for single-user transmission and analyzes the impact of the discrete aperture and polarization mismatch. Section IV proposes the VR detection algorithm, the user partition algorithm, and two low-complexity symbol detection algorithms. Section V presents the numerical results and Section VI concludes the paper.

Notations: Vectors and matrices are denoted by boldface lower case and upper case letters, respectively. The transpose, conjugate transpose, and inverse of matrix \mathbf{X} are denoted by \mathbf{X}^T , \mathbf{X}^H , and \mathbf{X}^{-1} , respectively. $[\mathbf{X}]_{(:,k)}$ denotes the k -th column of matrix \mathbf{X} . \mathcal{O} denotes the standard big-O notation. $|\mathcal{B}|$ denotes the cardinality of set \mathcal{B} . $\nabla_{\mathbf{x}} \times$ denotes the curl operation with respect to \mathbf{x} . Besides, \mathbf{I}_a denotes the identity matrix with a dimension of $a \times a$. The space of $a \times b$ complex matrices is denoted by $\mathbb{C}^{a \times b}$. The l_2 norm of a vector \mathbf{x} and the absolute value of a scalar x are denoted by $\|\mathbf{x}\|$ and $|x|$, respectively. j denotes the square root of -1 . $\lfloor a \rfloor$ denotes the

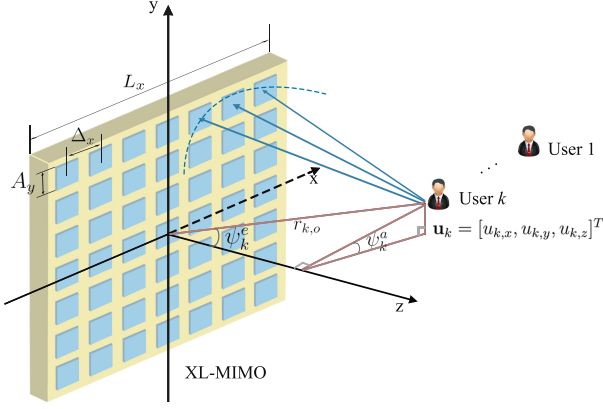


Fig. 1. Illustration of the considered XL-MIMO system.

nearest integer smaller than a .

II. SYSTEM MODEL

As illustrated in Fig. 1, we consider the uplink transmission from K single-antenna users to an XL-MIMO array. The user indices are collected in set $\mathcal{K} = \{1, \dots, K\}$. For tractability, we establish a coordinate system with the center of the array as the origin. The xoy plane is the plane in which the array lies, and the z -axis is perpendicular to the array. The location of user $k \in \mathcal{K}$ is denoted by $\mathbf{u}_k = [u_{k,x}, u_{k,y}, u_{k,z}]^T$.

A. XL-MIMO Array Structure

Unlike the works considering continuous surfaces or holographic surfaces [22]–[28], a discrete-aperture array model is adopted in this work. The XL-MIMO array consists of $M = M_x M_y$ antenna elements. The effective area of each antenna element is denoted by $A = A_x A_y$, where A_x and A_y are the lengths of the sides along the x - and y - axes, respectively¹. The antenna spacing along the x - and y - axes are denoted by Δ_x and Δ_y , respectively, with $\Delta_x > A_x$ and $\Delta_y > A_y$. Then, $\eta \triangleq \frac{A}{\Delta_x \Delta_y} \leq 1$ can be referred to as the array occupation ratio characterizing the impact of the discrete aperture of the XL-MIMO array. Considering the (m_x, m_y) -th antenna element, the coordinate of its center is given by $\mathbf{p}_{m_x, m_y} = [m_x \Delta_x, m_y \Delta_y, 0]^T$, $m_c \in \mathcal{M}_c$, where

$$\mathcal{M}_c = \{-(M_c - 1)/2, \dots, (M_c - 1)/2\}, c \in \{x, y\}. \quad (1)$$

Besides, the region covered by the effective area of the (m_x, m_y) -th antenna element is described as $S_{m_x, m_y} = [m_x \Delta_x - \frac{A_x}{2}, m_x \Delta_x + \frac{A_x}{2}] \times [m_y \Delta_y - \frac{A_y}{2}, m_y \Delta_y + \frac{A_y}{2}]$. The distance between user k and the center of the (m_x, m_y) -th array element is given by

$$\begin{aligned} r_{k, m_x, m_y} &= \|\mathbf{r}_{k, m_x, m_y}\| = \|\mathbf{p}_{m_x, m_y} - \mathbf{u}_k\| \\ &= \sqrt{(m_x \Delta_x - u_{k,x})^2 + (m_y \Delta_y - u_{k,y})^2 + (u_{k,z})^2}. \end{aligned} \quad (2)$$

¹To facilitate the analysis, we do not specify the form of the antennas (wire antennas, aperture antennas, etc.) on the array. We only focus on the effective area of the antenna [44], which enables us to establish a unified model. The result serves as an ideal case which is tractable to characterize the upper-bound performance of the communication system and draw insights.

The distance and the azimuth and elevation angles of arrival (AoAs) from user k to the array center are denoted by $r_{k,o} = \|\mathbf{u}_k\|$ and ψ_k^a and ψ_k^e , respectively, where $u_{k,x} = r_{k,o} \sin \psi_k^e \cos \psi_k^a$, $u_{k,y} = r_{k,o} \sin \psi_k^e \sin \psi_k^a$, and $u_{k,z} = r_{k,o} \cos \psi_k^e$.

B. Channel Modeling

Due to the near-field behavior, it is necessary to distinguish the power and phase of different elements when modeling the channel between the user and the XL-MIMO array. Specifically, the channel from user k to the (m_x, m_y) -th antenna element of the XL-MIMO array can be expressed in the following form:

$$h_{k, m_x, m_y} = \sqrt{\xi_{k, m_x, m_y}} e^{-j\chi_{k, m_x, m_y}}, \quad (3)$$

where ξ_{k, m_x, m_y} and χ_{k, m_x, m_y} are the channel power and phase, respectively. By merging h_{k, m_x, m_y} , $\forall m_x, m_y$, into a vector, the channel $\mathbf{h}_k \in \mathbb{C}^{M \times 1}$ from user k to the whole array can be obtained.

The Dyadic Green's function-based EM channel model is applied for modeling the power ξ_{k, m_x, m_y} and the phase χ_{k, m_x, m_y} of the channel h_{k, m_x, m_y} [23], [24], [45]. This channel model is more practical and allows the characterization of the impact of EM polarization effects. Specifically, consider a point $\mathbf{p} = [p_x, p_y, 0]^T$ located in the region covered by the (m_x, m_y) -th antenna element, i.e., $\mathbf{p} \in S_{m_x, m_y}$. Based on Maxwell's equations, the electric field due to the current source of user k satisfies the following inhomogeneous Helmholtz wave equation [23]

$$(-\nabla_{\mathbf{u}_k} \times \nabla_{\mathbf{u}_k} \times + k_0^2) \mathcal{E}(\mathbf{u}_k) = j k_0 \kappa \mathcal{J}(\mathbf{u}_k), \quad (4)$$

where $k_0 = \frac{2\pi}{\lambda}$, λ , and κ represent the wavenumber, the wavelength, and the intrinsic impedance of the free space, respectively. $\mathcal{E}(\mathbf{u}_k)$ is the electric field excited by the current density $\mathcal{J}(\mathbf{u}_k)$. The inverse mapping of (4) is given by $\mathcal{E}(\mathbf{p}) = \int \mathcal{G}(\mathbf{p}, \mathbf{u}_k) \mathcal{J}(\mathbf{u}_k) d\mathbf{u}_k$. In EM theory, $\mathcal{G}(\mathbf{p}, \mathbf{u}_k)$ is referred to as the Green function which in the radiating near field can be approximately given by [45]

$$\mathcal{G}(\mathbf{p}, \mathbf{u}_k) \approx \frac{-j\kappa}{2\lambda \|\mathbf{r}_k\|} (\mathbf{I}_3 - \hat{\mathbf{r}}_k \hat{\mathbf{r}}_k^H) e^{-j \frac{2\pi}{\lambda} \|\mathbf{r}_k\|}, \quad (5)$$

where $\mathbf{r}_k = \mathbf{p} - \mathbf{u}_k = [p_x - u_{k,x}, p_y - u_{k,y}, -u_{k,z}]^T$ and $\hat{\mathbf{r}}_k = \frac{\mathbf{r}_k}{\|\mathbf{r}_k\|}$. For notational simplicity, define $r_k = \|\mathbf{r}_k\|$ and hence $\hat{\mathbf{r}}_k = \left[\frac{p_x - u_{k,x}}{r_k}, \frac{p_y - u_{k,y}}{r_k}, \frac{-u_{k,z}}{r_k} \right]^T$. The Green function $\mathcal{G}(\mathbf{p}, \mathbf{u}_k)$ characterizes the EM response at point \mathbf{p} due to the current source at point \mathbf{u}_k . The current of the source can be decomposed into different polarization directions as $\mathcal{J}(\mathbf{u}_k) = \mathcal{J}_x(\mathbf{u}_k) \hat{\mathbf{e}}_x + \mathcal{J}_y(\mathbf{u}_k) \hat{\mathbf{e}}_y + \mathcal{J}_z(\mathbf{u}_k) \hat{\mathbf{e}}_z$, where $\hat{\mathbf{e}}_c$, $c \in \{x, y, z\}$, are the orthonormal basis vectors, and $\mathcal{J}_c(\mathbf{u}_k)$ denotes the current density in the c polarization direction. As in [23], [24], low-cost uni-polarized antenna elements are considered in this work and the excited current is assumed to flow in the positive y direction². Therefore, we have $\mathcal{J}(\mathbf{u}_k) = \mathcal{J}_y(\mathbf{u}_k) \hat{\mathbf{e}}_y$. For

²Cross-polarization components are neglected since their intensity could be 30 dB or more below the primary polarization [44].

unit density $\mathcal{J}_y(\mathbf{u}_k) = 1$, we have $\mathcal{J}(\mathbf{u}_k) = [0, 1, 0]^T$ and

$$\begin{aligned} \mathcal{G}(\mathbf{p}, \mathbf{u}_k) \mathcal{J}(\mathbf{u}_k) &\triangleq \mathcal{G}_y(\mathbf{r}_k) \\ &= \frac{-j\kappa}{2\lambda r_k} \left[\frac{(p_x - u_{k,x})(p_y - u_{k,y})}{r_k^2}, 1 - \left(\frac{p_y - u_{k,y}}{r_k} \right)^2, \right. \\ &\quad \left. \frac{(-u_{k,z})(p_y - u_{k,y})}{r_k^2} \right]^T e^{-j \frac{2\pi}{\lambda} \|\mathbf{r}_k\|}. \end{aligned} \quad (6)$$

Based on (6), we can model the channel power between user k and the (m_x, m_y) -th antenna element as follows

$$\xi_{k,m_x,m_y} = \int_{S_{m_x,m_x}} \frac{\lambda^2}{\kappa^2 \pi} \|\mathcal{G}_y(\mathbf{r}_k)\|^2 \frac{\mathbf{r}_k^T \hat{\mathbf{e}}_z}{\|\mathbf{r}_k\|} d\mathbf{p} \quad (7)$$

$$= \int_{S_{m_x,m_x}} \frac{1}{4\pi r_k^2} \frac{u_{k,z}}{r_k} \frac{(p_x - u_{k,x})^2 + u_{k,z}^2}{r_k^2} d\mathbf{p} \quad (8)$$

$$\mathbf{p} \approx \mathbf{p}_{m_x,m_y} \underset{\approx}{\sim} \frac{A}{4\pi} \frac{u_{k,z} \left((m_x \Delta_x - u_{k,x})^2 + u_{k,z}^2 \right)}{\left\{ (m_x \Delta_x - u_{k,x})^2 + (m_y \Delta_y - u_{k,y})^2 + u_{k,z}^2 \right\}^{\frac{5}{2}}}, \quad (9)$$

where (7) includes a normalized factor $\frac{\lambda^2}{\kappa^2 \pi}$ and a projection factor $\frac{\mathbf{r}_k^T \hat{\mathbf{e}}_z}{\|\mathbf{r}_k\|}$ that projects the signal from the incident direction onto the normal direction of the array to characterize the effective projected aperture [23], [24]. In (9), since the size of the antenna element is much smaller than the distance r_k , all points \mathbf{p} in the region S_{m_x,m_x} are approximated by the center point \mathbf{p}_{m_x,m_y} . Besides, by applying the approximation, $\mathbf{p} \approx \mathbf{p}_{m_x,m_y}$, to the phase of the Green function in (6), the phase of the channel between user k and the (m_x, m_y) -th antenna element can be obtained as³

$$\chi_{k,m_x,m_y} \approx \frac{2\pi}{\lambda} \|\mathbf{p}_{m_x,m_y} - \mathbf{u}_k\| = \frac{2\pi}{\lambda} r_{k,m_x,m_y}. \quad (10)$$

By substituting the channel power in (9) and the channel phase in (10) into the channel expression (3), the considered EM channel model is established.

From (8), we can observe that the modeled channel power is comprised of three components, including the free-space pathloss $\frac{1}{4\pi r_k^2}$, the projection coefficient $\frac{u_{k,z}}{r_k}$, and the polarization mismatch $\frac{(p_x - u_{k,x})^2 + u_{k,z}^2}{r_k^2}$ [24]. Clearly, if the signal is vertically incident, we have $u_{k,x} = u_{k,y} = 0$ and $\frac{u_{k,z}}{r_k} = 1$; if $u_{k,y} = p_y$, then $\frac{(p_x - u_{k,x})^2 + u_{k,z}^2}{r_k^2} = 1$ and (9) simplifies to the case without polarization mismatch as in [30, (2)]. Meanwhile, it can be seen that the expression of the channel phase is more complicated than that used in the far field [46]. Thus, the utilized EM channel model is more general and allows us to provide insights into the impact of polarization⁴.

III. SNR ANALYSIS FOR SINGLE-USER SCENARIO

To gain useful insights for system design, in this section, we first focus on a single-user scenario, i.e., $K = 1$. We

³Based on the reciprocity theorem for antennas and EM theory, the obtained channel model also holds for the downlink communication [44].

⁴The mutual coupling between different antennas and the return loss are neglected by assuming the ideal decoupling technique and hardware design. The general modeling with antenna coupling is valuable and will be left for our future work.

assume that only user k exists. Our objective is to derive an explicit expression for the SNR and analyze its properties in the context of near-field transmission. The signal received at the XL-MIMO array is expressed as $\mathbf{y}_k = \sqrt{p} \mathbf{h}_k x_k + \mathbf{n}$, where p is the transmit power, $x_k \sim \mathcal{CN}(0, 1)$ is the transmit symbol of user k , and $\mathbf{n} \sim \mathcal{CN}(\mathbf{0}, \sigma^2 \mathbf{I}_M)$. Using an MRC detector, the SNR is calculated as

$$\text{SNR}_k = \frac{p}{\sigma^2} \|\mathbf{h}_k\|^2 = \frac{p}{\sigma^2} \sum_{m_x \in \mathcal{M}_x} \sum_{m_y \in \mathcal{M}_y} \xi_{k,m_x,m_y}, \quad (11)$$

where ξ_{k,m_x,m_y} is given in (9). In the following, we will present an explicit expression of (11) instead of utilizing the double-sum format.

Theorem 1 *Considering channel model (3) and user k with location $\mathbf{u}_k = [u_{k,x}, u_{k,y}, u_{k,z}]^T$, if $u_{k,z} = 0$, we have $\text{SNR}_k = 0$; otherwise, the SNR is given by*

$$\begin{aligned} \text{SNR}_k = \frac{p}{\sigma^2} \frac{\eta}{6\pi} &\left\{ F_k \left(\frac{M_y \Delta_y}{2} - u_{k,y}, \frac{M_x \Delta_x}{2} - u_{k,x} \right) \right. \\ &+ F_k \left(\frac{M_y \Delta_y}{2} - u_{k,y}, \frac{M_x \Delta_x}{2} + u_{k,x} \right) \\ &+ F_k \left(\frac{M_y \Delta_y}{2} + u_{k,y}, \frac{M_x \Delta_x}{2} - u_{k,x} \right) \\ &\left. + F_k \left(\frac{M_y \Delta_y}{2} + u_{k,y}, \frac{M_x \Delta_x}{2} + u_{k,x} \right) \right\}, \end{aligned} \quad (12)$$

where $F_k(a, b) = \arctan \left(\frac{a}{u_{k,z}} \frac{b}{\sqrt{b^2 + a^2 + u_{k,z}^2}} \right) + \frac{u_{k,z}}{2} \frac{a}{a^2 + u_{k,z}^2} \frac{b}{\sqrt{b^2 + a^2 + u_{k,z}^2}}$.

Proof: See Appendix A. ■

Denote L_x and L_y as the physical dimensions of the XL-MIMO array along the x - and y -axes, respectively. For large M , we have $(L_x - M_x \Delta_x)/L_x \approx 0$ and $(L_y - M_y \Delta_y)/L_y \approx 0$. Therefore the SNR in (12) can be further approximated as

$$\begin{aligned} \text{SNR}_k = \frac{p}{\sigma^2} \frac{\eta}{6\pi} &\left\{ F_k \left(\frac{L_y}{2} - u_{k,y}, \frac{L_x}{2} - u_{k,x} \right) \right. \\ &+ F_k \left(\frac{L_y}{2} - u_{k,y}, \frac{L_x}{2} + u_{k,x} \right) \\ &+ F_k \left(\frac{L_y}{2} + u_{k,y}, \frac{L_x}{2} - u_{k,x} \right) \\ &\left. + F_k \left(\frac{L_y}{2} + u_{k,y}, \frac{L_x}{2} + u_{k,x} \right) \right\}. \end{aligned} \quad (13)$$

The SNR in (13) is a function of array lengths L_x, L_y , user location \mathbf{u}_k , and array occupation ratio $\eta = \frac{A}{\Delta_x \Delta_y} \leq 1$. Coefficient η highlights the difference of discrete-aperture arrays compared with continuous-aperture arrays. The SNR is an increasing function of η since $\eta L_x L_y$ represents the effective array aperture. Next, we aim to analyze the impact of polarization mismatch on the SNR when using a discrete array. Substituting $\frac{(p_x - u_{k,x})^2 + u_{k,z}^2}{r_k^2} = 1$ into (8), we can obtain

the SNR without polarization mismatch as follows

$$\begin{aligned} \text{SNR}_k^{w/o} = & \frac{p}{\sigma^2} \frac{\eta}{6\pi} \left\{ F_k^{w/o} \left(\frac{L_y}{2} - u_{k,y}, \frac{L_x}{2} - u_{k,x} \right) \right. \\ & + F_k^{w/o} \left(\frac{L_y}{2} + u_{k,y}, \frac{L_x}{2} - u_{k,x} \right) \\ & + F_k^{w/o} \left(\frac{L_y}{2} - u_{k,y}, \frac{L_x}{2} + u_{k,x} \right) \\ & \left. + F_k^{w/o} \left(\frac{L_y}{2} + u_{k,y}, \frac{L_x}{2} + u_{k,x} \right) \right\}, \end{aligned} \quad (14)$$

where $F_k^{w/o}(a, b) = \frac{3}{2} \arctan \left(\frac{ab}{u_{k,z} \sqrt{a^2 + b^2 + u_{k,z}^2}} \right)$. Note that by dividing each term in (14) by $r_{k,o}$ and switching the x -axis and y -axis, this result is identical to that in [30, (12)]. Comparing (13) with (14), we note that function $F_k(a, b)$ is more complex than $F_k^{w/o}(a, b)$, rendering the theoretical analysis more challenging. Recall the assumption of a y -axis polarization direction. As a result, the polarization mismatch escalates with the divergence between the y -coordinate of the user and the antenna element. Thus, when $L_y \rightarrow \infty$ (in the severe near field), we can show that $\text{SNR}_k \rightarrow \frac{2}{3} \text{SNR}_k^{w/o}$, which unveils the possible performance degradation attributed to polarization mismatch. Besides, for large $u_{k,z}$ (in the far field), we have $\arctan \left(\frac{a}{u_{k,z}} \frac{b}{\sqrt{b^2 + a^2 + u_{k,z}^2}} \right) \approx \frac{ab}{u_{k,z} \sqrt{b^2 + a^2 + u_{k,z}^2}}$ and $\frac{u_{k,z}}{2} \frac{a}{a^2 + u_{k,z}^2} \frac{b}{\sqrt{b^2 + a^2 + u_{k,z}^2}} \approx \frac{ab}{2u_{k,z} \sqrt{b^2 + a^2 + u_{k,z}^2}}$, which results in $F_k(a, b) \approx F_k^{w/o}(a, b)$ and accordingly $\text{SNR}_k \approx \text{SNR}_k^{w/o} \approx \frac{p}{\sigma^2} \frac{1}{4\pi r_{k,o}^2} M A \cos \psi_k^e$ [30]. This shows that the polarization mismatch plays a more important role in the near field, and its impact is highly dependent on parameter a , i.e., L_y and $u_{k,y}$.

In addition, it is worth noting that the SNR in (13) can be also understood from the perspective of the 3D angles. Define $\Psi_{k,x} \triangleq \frac{u_{k,x}}{r_{k,o}} = \sin \psi_k^e \cos \psi_k^a$, $\Psi_{k,y} \triangleq \frac{u_{k,y}}{r_{k,o}} = \sin \psi_k^e \sin \psi_k^a$, and $\Psi_{k,z} \triangleq \frac{u_{k,z}}{r_{k,o}} = \cos \psi_k^e$. Then, the SNR can be reformulated as a function of the AoAs and $r_{k,o}$ as follows:

$$\begin{aligned} \text{SNR}_k = & \frac{p}{\sigma^2} \frac{\eta}{6\pi} \left\{ F_k^A \left(\frac{L_y}{2r_{k,o}} - \Psi_{k,y}, \frac{L_x}{2} - \Psi_{k,x} \right) \right. \\ & + F_k^A \left(\frac{L_y}{2r_{k,o}} - \Psi_{k,y}, \frac{L_x}{2} + \Psi_{k,x} \right) \\ & + F_k^A \left(\frac{L_y}{2r_{k,o}} + \Psi_{k,y}, \frac{L_x}{2} - \Psi_{k,x} \right) \\ & \left. + F_k^A \left(\frac{L_y}{2r_{k,o}} + \Psi_{k,y}, \frac{L_x}{2} + \Psi_{k,x} \right) \right\}, \end{aligned} \quad (15)$$

where $F_k^A(a, b) = \arctan \left(\frac{a}{\Psi_{k,z}} \frac{b}{\sqrt{b^2 + a^2 + \Psi_{k,z}^2}} \right) + \frac{\Psi_{k,z}}{2} \frac{a}{a^2 + \Psi_{k,z}^2} \frac{b}{\sqrt{b^2 + a^2 + \Psi_{k,z}^2}}$.

A. Asymptotic Limit

In massive MIMO systems operating under far-field conditions and subject to free-space pathloss [2], the SNR in the single-user case is given by $\text{SNR}_k^{\text{far}} = \frac{p}{\sigma^2} \frac{\lambda^2}{(4\pi)^2 r_{k,o}^2} M$, which

grows linearly with M towards infinity. However, in reality, the received power cannot exceed the transmitted power based on energy conservation. In fact, when $M \rightarrow \infty$, the near-field channel model has to be applied and the linear scale in $\text{SNR}_k^{\text{far}}$ no longer holds. Based on the EM near-field channel, when $M \rightarrow \infty$, the SNR in (12) converges to

$$\text{SNR}_k \rightarrow \frac{p}{\sigma^2} \frac{4\eta}{6\pi} F_k \left(\frac{L_y}{2}, \frac{L_x}{2} \right) \rightarrow \frac{p}{\sigma^2} \frac{\eta}{3}. \quad (16)$$

If the polarization mismatch is neglected, the asymptotic SNR becomes

$$\text{SNR}_k^{w/o} \rightarrow \frac{p}{\sigma^2} \frac{\eta}{\pi} F_k^{w/o} \left(\frac{L_y}{2}, \frac{L_x}{2} \right) \rightarrow \frac{p}{\sigma^2} \frac{\eta}{2}. \quad (17)$$

If the array is assumed to be continuous i.e., $A_x = \Delta_x$ and $A_y = \Delta_y$, we have

$$\text{SNR}_k^{\text{cont}} \rightarrow \frac{p}{\sigma^2} \frac{1}{3}. \quad (18)$$

The results in (16) - (18) provide the practical performance limit for XL-MIMO with an infinitely large array area. As can be observed, the SNR in (16) is smaller than the other two cases in (17) and (18). In (17), at most half of the power can be received by an infinitely large array surface, since it can capture only the power emitting into half of the space. With polarization mismatch, the limit reduces from 1/2 to 1/3. This is because as L_y increases, the attenuation of the amplitude from the source to the edge of the array becomes severer in the presence of polarization mismatch, and therefore an additional loss is caused. For the considered discrete aperture, the asymptotic SNR performance is additionally constrained by the array occupation ratio η since it characterizes the effective aperture of the array capable of receiving a signal.

The reason why the SNR is limited as $M \rightarrow \infty$ can be explained more clearly from the perspective of geometric views. Consider a user located perpendicular to the center of the array, i.e., $u_{k,x} = u_{k,y} = 0$. Then, the SNR becomes

$$\begin{aligned} \text{SNR}_k^{\text{P}} = & \frac{p}{\sigma^2} \frac{2\eta}{3\pi} \left\{ \arctan \left(\frac{L_y/2}{u_{k,z}} \frac{L_x/2}{\sqrt{\left(\frac{L_x}{2}\right)^2 + \left(\frac{L_y}{2}\right)^2 + u_{k,z}^2}} \right) \right. \\ & \left. + \frac{1}{2} \frac{u_{k,z}}{\sqrt{\left(\frac{L_x}{2}\right)^2 + u_{k,z}^2}} \frac{L_y/2}{\sqrt{\left(\frac{L_y}{2}\right)^2 + u_{k,z}^2}} \frac{L_x/2}{\sqrt{\left(\frac{L_x}{2}\right)^2 + \left(\frac{L_y}{2}\right)^2 + u_{k,z}^2}} \right\}. \end{aligned} \quad (19)$$

Eq. (19) can be reformulated in the form of geometric angles. As illustrated in Fig. 2, we define two angles α and β so that $\tan \alpha = \frac{L_y/2}{u_{k,z}}$ and $\cos \beta = \frac{L_x/2}{\sqrt{\left(\frac{L_x}{2}\right)^2 + \left(\frac{L_y}{2}\right)^2 + u_{k,z}^2}}$.

Then, we have

$$\text{SNR}_k^{\text{P}} = \frac{p}{\sigma^2} \frac{2\eta}{3\pi} \left\{ \arctan(\tan \alpha \cos \beta) + \frac{1}{2} \sin \alpha \cos \alpha \cos \beta \right\}. \quad (20)$$

The SNR in (20) is a function of angles α and β . Even as the array aperture expands to an infinitely large extent, the angles of view from the user to the array, i.e., α and β , remain limited. Specifically, if $L_x \rightarrow \infty$, we have $\beta \rightarrow 0$. When $L_y \rightarrow \infty$, we have $\alpha, \beta \rightarrow \frac{\pi}{2}$. If both L_x and L_y tend to infinity, the angles

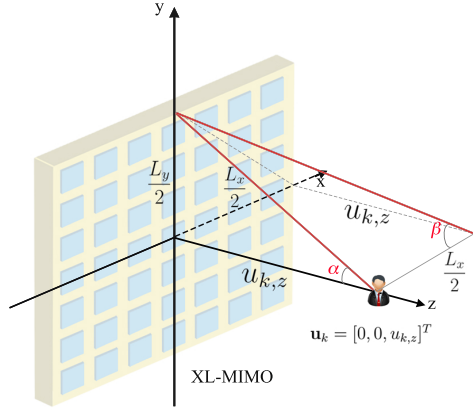


Fig. 2. Geometric interpretation of the SNR.

converge to $\alpha \rightarrow \frac{\pi}{2}$ and $\beta \rightarrow \frac{\pi}{4}$. As a result, the SNR is limited by the angles of view and cannot increase unboundedly.

B. XL-ULA

To shed more light on the impact of polarization mismatch, in this section, we consider a simplified case where the XL-UPA simplifies to an XL-ULA, i.e., $M_x = 1$ or $M_y = 1$.

Theorem 2 When $M_y = 1$, the SNR for the XL-ULA simplifies to

$$\text{SNR}_k^{\text{ULA}} = \frac{p}{\sigma^2} \frac{A}{4\pi\Delta_x} \left\{ F_k^{\text{ULA}} \left(\frac{M_x\Delta_x}{2} - u_{k,x} \right) + F_k^{\text{ULA}} \left(\frac{M_x\Delta_x}{2} + u_{k,x} \right) \right\}, \quad (21)$$

$$\text{where } F_k^{\text{ULA}}(a) = \frac{a(a^2 u_{k,y}^2 + 3u_{k,z}^2 (a^2 + u_{k,y}^2 + u_{k,z}^2)) u_{k,z}}{3(u_{k,y}^2 + u_{k,z}^2)^2 (a^2 + u_{k,y}^2 + u_{k,z}^2)^{\frac{3}{2}}}.$$

Proof: See Appendix B. ■

The result in (21) is consistent with [30] only if we have $u_{k,y} = 0$. This is because when $M_y = 1$, the y -coordinate of all antenna elements of the XL-ULA is 0. When the y -coordinate of the user is also $u_{k,y} = 0$, the difference of y -coordinate of the user and all antennas elements becomes zero, and therefore, there will be no polarization mismatch in pathloss (9). For $M_x \rightarrow \infty$, the asymptotic limit of the SNR in (21) is given by

$$\text{SNR}_k^{\text{ULA}} \xrightarrow{M \rightarrow \infty} \frac{p}{\sigma^2} \frac{A}{2\pi\Delta_x} \frac{u_{k,z} (u_{k,y}^2 + 3u_{k,z}^2)}{3(u_{k,y}^2 + u_{k,z}^2)^2}. \quad (22)$$

As can be seen, (22) is independent of $u_{k,x}$. This is because as $M_x \rightarrow \infty$, the array attains an infinite length, rendering the user's x -coordinate inconsequential. Furthermore, the asymptotic SNR for the XL-ULA without polarization mismatch is

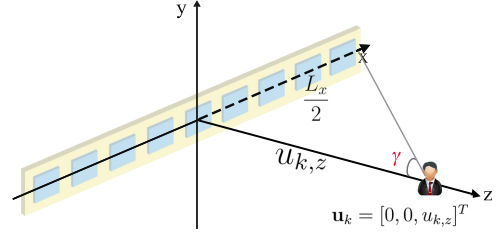


Fig. 3. Geometric interpretation in the case of XL-ULA.

given by

$$\begin{aligned} \text{SNR}_{k,w/o}^{\text{ULA}} &\xrightarrow{M \rightarrow \infty} \frac{p}{\sigma^2} \frac{A}{2\pi\Delta_x} \frac{u_{k,z}}{u_{k,y}^2 + u_{k,z}^2} \\ &= \frac{p}{\sigma^2} \frac{A}{2\pi\Delta_x} \frac{u_{k,z} (3u_{k,y}^2 + 3u_{k,z}^2)}{3(u_{k,y}^2 + u_{k,z}^2)^2} \geq \text{SNR}_k^{\text{ULA}}, \end{aligned} \quad (23)$$

and the gap between (22) and (23) is

$$D_{\text{SNR}_k} = \text{SNR}_{k,w/o}^{\text{ULA}} - \text{SNR}_k^{\text{ULA}} = \frac{p}{\sigma^2} \frac{A}{3\pi\Delta_x} \frac{u_{k,z} u_{k,y}^2}{(u_{k,y}^2 + u_{k,z}^2)^2}, \quad (24)$$

which first increases and then decreases with respect to $u_{k,y}$. Specifically, we have $D_{\text{SNR}_k} \rightarrow 0$ as $u_{k,y} \rightarrow 0$ and $u_{k,y} \rightarrow \infty$. This is because when $u_{k,y} = 0$, the user possesses the same y -coordinate as the whole ULA, and therefore the polarization mismatch vanishes. As $u_{k,y}$ increases, the discrepancy in the y -coordinate widens, leading to a larger polarization mismatch. For large enough $u_{k,y}$, the user will be located in the far field and therefore the gap vanishes.

Besides, for $u_{k,x} = u_{k,y} = 0$, we can rewrite the SNR expression in (21) as follows

$$\begin{aligned} \text{SNR}_k^{\text{ULA}} &= \frac{p}{\sigma^2} \frac{A}{2\pi\Delta_x u_{k,z}} \left(\frac{L_x/2}{\sqrt{(L_x/2)^2 + u_{k,z}^2}} \right)^3 \\ &= \frac{p}{\sigma^2} \frac{A}{2\pi\Delta_x u_{k,z}} (\sin \gamma)^3, \end{aligned} \quad (25)$$

where γ denotes half of the view angle from the user to the ULA as illustrated in Fig. 3. Obviously, when $M_x \rightarrow \infty$, we have $\gamma \rightarrow \frac{\pi}{2}$, and therefore the SNR is limited.

C. Near-Field/Far-Field Boundary

In this section, we examine the boundary differentiating the near and far fields for the considered discrete array with an EM channel model. A classic result for distinguishing the near and far fields is the Fraunhofer distance [16], [20], [47], i.e., $d_f = \frac{2D^2}{\lambda}$, where D is the largest array aperture. It states that if the distance is larger than d_f , the maximal phase error of the received signal across the array resulting from approximating the spherical wavefront to the planar wavefront, would be smaller than $\frac{\pi}{8}$ radians. This result has some limits. Firstly, it is obtained based on the condition $\psi_k^e = \psi_k^a = 0$, meaning it applies only to signals impinging perpendicularly on the center of the array. Therefore, the impact of the direction

of the incident signal is not captured. Secondly, this result only distinguishes the near and far fields according to the signal phase. However, the near and far fields also differ in the feature of the signal power as analyzed in Section III-A. Finding the boundary distinguishing the near and far fields based on the variation of the signal power across the array is also of practical importance. Therefore, a more general field boundary is needed by taking into consideration the impact of incident signal directions and the variation of the signal power across the array.

In the following, we will first determine the field boundary based on the signal phase (with any incident directions) and signal power, respectively, and finally discuss the general result.

1) *Near-field region characterized by phase error with arbitrary incident directions:* To begin with, we complement the classic Fraunhofer distance by further considering arbitrary incident signal directions (i.e., $\forall \psi_k^e, \psi_k^a$). To this end, we commence by deriving the maximal phase error across the array as a function of signal directions. Recall that the phase of the channel between user k and the (m_x, m_y) -th antenna elements is $\chi_{k,m_x,m_y} = \frac{2\pi}{\lambda} r_{k,m_x,m_y}$ where the distance r_{k,m_x,m_y} in (2) can be reformulated as (26) shown at the bottom of the page, with $\Psi_{k,x} = \frac{u_{k,x}}{r_{k,o}} = \sin \psi_k^e \cos \psi_k^a$ and $\Psi_{k,y} = \frac{u_{k,y}}{r_{k,o}} = \sin \psi_k^e \sin \psi_k^a$. Then, based on the second-order Taylor approximation $(1+x)^{\frac{1}{2}} \approx 1 + \frac{1}{2}x - \frac{1}{8}x^2$ [48] and neglecting the terms of $\mathcal{O}(r_{k,o}^{-2})$ and $\mathcal{O}(r_{k,o}^{-3})$, we obtain (27), shown at the bottom of the page.

Note that based on the first-order Taylor approximation of r_{k,m_x,m_y} in (26), the phase of the channel between user k and the (m_x, m_y) -th antenna element *in the far field* is expressed as $\chi_{k,m_x,m_y}^{\text{far}} = \frac{2\pi}{\lambda} (r_{k,o} - (m_x \Delta_x \Psi_{k,x} + m_y \Delta_y \Psi_{k,y}))$. Then, the 3D near-/far-field boundary characterized by phase error is obtained in the following theorem.

Theorem 3 *The phase error-based 3D near-/far-field boundary is comprised of the coordinates $\tilde{\mathbf{u}}_k = [\tilde{r}_{k,o} \Psi_{k,x}, \tilde{r}_{k,o} \Psi_{k,y}, \tilde{r}_{k,o} \Psi_{k,z}]$, where the values of $\tilde{r}_{k,o}$, for all directions $\psi_k^e \in [0, \frac{\pi}{2}]$, $\psi_k^a \in [0, 2\pi]$, are given by (28) shown at the bottom of the next page.*

Proof: Based on (27), the fact $\Psi_{k,x}^2, \Psi_{k,y}^2 < 1$, and the domains of m_x, m_y in (1), the maximal phase error across the whole array is derived as (29) shown at the bottom of the next page, where the maximal value is achieved by either $(m_x, m_y) = (\frac{M_x-1}{2}, \frac{M_y-1}{2})$ or $(m_x, m_y) =$

$(-\frac{M_x-1}{2}, \frac{M_y-1}{2})$. It can be seen that $D_{\chi_{k,m_x,m_y}}$ decreases with $r_{k,o}$ given any directions (ψ_k^e, ψ_k^a) . Therefore, $\tilde{r}_{k,o}$ in (28) is obtained by letting $D_{\chi_{k,m_x,m_y}} = \frac{\pi}{8}$. ■

The distance in (28) degrades to classic Fraunhofer distance under the perpendicular incident direction, i.e., $(\psi_k^e, \psi_k^a) = (0, 0)$. Specifically, applying $\Psi_{k,x} = \Psi_{k,y} = 0$, $\frac{M_x-1}{2} \Delta_x \approx L_x$, and $\frac{M_y-1}{2} \Delta_y \approx L_y$ into (28), we have $\tilde{r}_{k,o}^p \approx \frac{8}{\lambda} \left\{ (L_x/2)^2 + (L_y/2)^2 \right\} = 2D^2/\lambda$ which is identical to the classical result in [16]. Theorem 3 proves that for any signal incident directions, the near-field distance $\tilde{r}_{k,o}$ always increases with M , i.e., the physical dimensions of the array. Besides, with the square array of $M_x \Delta_x = M_y \Delta_y \approx L$, we have

$$\begin{aligned} \tilde{r}_{k,o}^s &\approx \frac{2L^2}{\lambda} \left(2 - (|\Psi_{k,x}| - |\Psi_{k,y}|)^2 \right) \\ &= \frac{D^2}{\lambda} \left(2 - |\sin \psi_k^e|^2 (|\cos \psi_k^a| - |\sin \psi_k^a|)^2 \right) \leq \frac{2D^2}{\lambda}. \end{aligned} \quad (30)$$

(30) reveals that the near-field distance with different incident directions is smaller than the classical Fraunhofer distance. Besides, it can be found that $\tilde{r}_{k,o}^s$ decreases with ψ_k^e . Therefore, given ψ_k^a , the phase error-based near-field region shrinks as ψ_k^e increases from 0 to $\pi/2$, which showcases the impact of the incident signal direction on the field boundary.

2) *Near-field region characterized by power variations:* As shown in (11), with the MRC, it is the power variation across the array differentiating the SNR performance in the near field and far field. Therefore, it is meaningful to identify the near-field region in which the power variation across different antenna elements is non-negligible. Inspired by [30], the degree of the variation of the channel powers across the whole array based on the EM channel model can be quantified as

$$v(\mathbf{u}_k) = \frac{\min_{m_x, m_y} \xi_{k,m_x, m_y}}{\max_{m_x, m_y} \xi_{k,m_x, m_y}}. \quad (31)$$

For \mathbf{u}_k located in the far field with planar wavefront, the power variation across the array can be neglected and we have $v(\mathbf{u}_k) \approx 1$. As the user moves closer to the array, the near-field behavior manifests itself, and the variation of the power across the array becomes non-negligible. Intuitively, the value of $v(\mathbf{u}_k)$ decreases from 1 to 0 as the user moves closer and closer to the array. Therefore, we can determine the near-field region by finding the locations of \mathbf{u}_k so that $v(\mathbf{u}_k) < \bar{v}_t$, where \bar{v}_t is a threshold explaining the maximal acceptable degree of power difference across the whole array in the far

$$r_{k,m_x, m_y} = r_{k,o} \sqrt{1 + \frac{-(2m_x \Delta_x r_{k,o} \Psi_{k,x} + 2m_y \Delta_y r_{k,o} \Psi_{k,y}) + (m_x \Delta_x)^2 + (m_y \Delta_y)^2}{r_{k,o}^2}}, \quad (26)$$

$$r_{k,m_x, m_y} \approx r_{k,o} - (m_x \Delta_x \Psi_{k,x} + m_y \Delta_y \Psi_{k,y}) + \frac{(m_x \Delta_x)^2 (1 - \Psi_{k,x}^2) + (m_y \Delta_y)^2 (1 - \Psi_{k,y}^2) - 2\Delta_x \Delta_y \Psi_{k,x} \Psi_{k,y} m_x m_y}{2r_{k,o}}. \quad (27)$$

field.

To avoid the exhausting search across the array, in the following, we will provide the closed-form expressions of the variables (m_x, m_y) in (31) which maximize and minimize ξ_{k, m_x, m_y} given \mathbf{u}_k , respectively. Based on (9), we can find that the power ξ_{k, m_x, m_y} between user k and the (m_x, m_y) -th antenna element decreases with their y -coordinate difference $|m_y \Delta_y - u_{k,y}|$ but it is not monotonic of their x -coordinate difference $|m_x \Delta_x - u_{k,x}|$. This is because when $|m_y \Delta_y - u_{k,y}|$ increases, both the distance and the polarization mismatch increase. By contrast, when $|m_x \Delta_x - u_{k,x}|$ increases, the distance increases but the relative polarization mismatch decreases. By defining $s = (m_x \Delta_x - u_{k,x})^2 + u_{k,z}^2$ and $v = (m_y \Delta_y - u_{k,y})^2$, we can rewrite ξ_{k, m_x, m_y} in (9) as $f_\xi(s) = \frac{s}{(s+v)^{\frac{3}{2}}}$ with $f'_\xi(s) = (s+v)^{-\frac{7}{2}}(v - \frac{3}{2}s)$. For notational simplicity, define $f_{\text{int}}(a) = \lfloor a + \frac{1}{2} \rfloor$ as the function rounding a to the nearest integer. Define further $f_{\pm x}(a) = \frac{u_{k,x}}{|u_{k,x}|} a$, and $f_{|\min|}(a, b)$, where $f_{|\min|}(a, b) = a$ if $|a| \leq |b|$ and $f_{|\min|}(a, b) = b$ if $|a| > |b|$. Then, based on the range in (1), we can derive the domain of $s \in [s_{\min}, \dots, s_{\max}]$, where $s_{\max} = (f_{\pm x}(\frac{M_x-1}{2}) \Delta_x + u_{k,x})^2 + u_{k,z}^2$ and⁵

$$s_{\min} = \left(\left\{ f_{|\min|} \left(f_{\text{int}} \left(\frac{u_{k,x}}{\Delta_x} \right), f_{\pm x} \left(\frac{M_x-1}{2} \right) \right) \right\} \Delta_x - u_{k,x} \right)^2 + u_{k,z}^2. \quad (32)$$

By analyzing the properties of $f_\xi(s)$, we obtain the following solutions: to maximize $f_\xi(s)$, we have $\overline{m}_y = f_{|\min|} \left\{ f_{\text{int}} \left(\frac{u_{k,y}}{\Delta_y} \right), f_{\pm y} \left(\frac{M_y-1}{2} \right) \right\}$, $v^* = (\overline{m}_y \Delta_y - u_{k,y})^2$, and

$$\overline{m}_x = \begin{cases} f_{\text{int}} \left(f_{|\min|} \left\{ \frac{\sqrt{\frac{2}{3}v^* - u_{k,z}^2 + u_{k,x}}}{\Delta_x}, \frac{-\sqrt{\frac{2}{3}v^* - u_{k,z}^2 + u_{k,x}}}{\Delta_x} \right\} \right), & \text{if } s_{\min} \leq \frac{2}{3}v^* \leq s_{\max}; \\ f_{|\min|} \left\{ f_{\text{int}} \left(\frac{u_{k,x}}{\Delta_x} \right), f_{\pm x} \left(\frac{M_x-1}{2} \right) \right\}, & \text{if } \frac{2}{3}v^* < s_{\min}; \\ -f_{\pm x} \left(\frac{M_x-1}{2} \right), & \text{if } \frac{2}{3}v^* > s_{\max}; \end{cases} \quad (33)$$

⁵For brevity, we assume that M is odd, and the case of even values can be tackled in a similar manner.

to minimize $f_\xi(s)$, we have $\underline{m}_y = -f_{\pm y} \left(\frac{M_y-1}{2} \right)$, $v^* = (\underline{m}_y \Delta_y - u_{k,y})^2$, and

$$\underline{m}_x = \begin{cases} f_{|\min|} \left\{ f_{\text{int}} \left(\frac{u_{k,x}}{\Delta_x} \right), f_{\pm x} \left(\frac{M_x-1}{2} \right) \right\}, & \text{if } s_{\min} \leq \frac{2}{3}v^* \leq s_{\max}, f_\xi(s_{\min}) \leq f_\xi(s_{\max}); \\ -f_{\pm x} \left(\frac{M_x-1}{2} \right), & \text{if } s_{\min} \leq \frac{2}{3}v^* \leq s_{\max}, f_\xi(s_{\min}) > f_\xi(s_{\max}); \\ f_{|\min|} \left\{ f_{\text{int}} \left(\frac{u_{k,x}}{\Delta_x} \right), f_{\pm x} \left(\frac{M_x-1}{2} \right) \right\}, & \text{if } \frac{2}{3}v^* > s_{\max}; \\ -f_{\pm x} \left(\frac{M_x-1}{2} \right), & \text{if } \frac{2}{3}v^* < s_{\min}. \end{cases} \quad (34)$$

Based on (33) and (34), we can calculate $\mathbf{v}(\mathbf{u}_k)$ given \mathbf{u}_k . To find the $\tilde{\mathbf{u}}_k = [\tilde{u}_{k,x}, \tilde{u}_{k,y}, \tilde{u}_{k,z}]$ on the near/far-field boundary, we can fix $\tilde{u}_{k,x}$ and $\tilde{u}_{k,y}$ and then use a one-dimensional search to find the required value of $\tilde{u}_{k,z}$ which leads to $\mathbf{v}(\tilde{\mathbf{u}}_k) = \bar{\mathbf{v}}_t$.

3) *The general phase- and power-based near-/far-field boundary:* In the above discussions, we have introduced the phase-based and power-based field boundaries, respectively. These two field boundaries delineate the near-field regions in which the near-field behaviors are evident in terms of the signal phase and signal power, respectively. Consequently, the union of these two regions describes the near-field region beyond which both the power variations and phase errors are slight and the near-field spherical wavefront can be approximated as the far-field planar wavefront with negligible errors. Conversely, the intersection of these two regions characterizes the near-field region inside which both the power variations and phase errors across the whole array are pronounced.

IV. MULTI-USER SCENARIO

Based on the single-user case, the previous section has shed light on the performance and properties of XL-MIMO in the near field. Next, this section focuses on the general multi-user scenarios and proposes low-complexity symbol detectors by leveraging the near-field properties.

A. Whole Array-Based Design

The signal received by the XL-MIMO array from the K users can be expressed as $\mathbf{y} = \sqrt{\rho} \mathbf{H} \mathbf{x} + \mathbf{n}$, where $\mathbf{H} =$

$$\tilde{r}_{k,o} = \frac{\left(\frac{M_x-1}{2} \Delta_x \right)^2 \left(1 - \Psi_{k,x}^2 \right) + \left(\frac{M_y-1}{2} \Delta_y \right)^2 \left(1 - \Psi_{k,y}^2 \right) + 2 \Delta_x \Delta_y |\Psi_{k,x} \Psi_{k,y}| \frac{M_x-1}{2} \frac{M_y-1}{2}}{\lambda/8}. \quad (28)$$

$$\begin{aligned} D_{\chi_{k, m_x, m_y}} &= \max_{m_x, m_y} \left(\chi_{k, m_x, m_y} - \chi_{k, m_x, m_y}^{\text{far}} \right) \\ &\approx \max_{m_x, m_y} \frac{2\pi (m_x \Delta_x)^2 \left(1 - \Psi_{k,x}^2 \right) + (m_y \Delta_y)^2 \left(1 - \Psi_{k,y}^2 \right) - 2 \Delta_x \Delta_y \Psi_{k,x} \Psi_{k,y} m_x m_y}{\lambda} \\ &= \frac{\pi \left(\frac{M_x-1}{2} \Delta_x \right)^2 \left(1 - \Psi_{k,x}^2 \right) + \left(\frac{M_y-1}{2} \Delta_y \right)^2 \left(1 - \Psi_{k,y}^2 \right) + 2 \Delta_x \Delta_y |\Psi_{k,x} \Psi_{k,y}| \frac{M_x-1}{2} \frac{M_y-1}{2}}{\lambda}, \end{aligned} \quad (29)$$

$[\mathbf{h}_1, \dots, \mathbf{h}_K]$ and $\mathbf{x} = [x_1, \dots, x_K]$. Define $\bar{\mathbf{H}}_k = [\mathbf{H}]_{(:, \mathcal{K} \setminus k)}$ as the matrix obtained by excluding the k -th column from \mathbf{H} . Then, to detect x_k , the linear MRC, ZF, and MMSE detectors for user k are given by [31], [49]

$$\mathbf{a}_{k,\text{MRC}}^H = \frac{\mathbf{h}_k^H}{\|\mathbf{h}_k\|^2}, \quad (35)$$

$$\mathbf{a}_{k,\text{ZF}}^H = \frac{\mathbf{h}_k^H \mathbf{P}_k}{\mathbf{h}_k^H \mathbf{P}_k \mathbf{h}_k}, \mathbf{P}_k = \mathbf{I}_M - \bar{\mathbf{H}}_k \left(\bar{\mathbf{H}}_k^H \bar{\mathbf{H}}_k \right)^{-1} \bar{\mathbf{H}}_k^H, \quad (36)$$

$$\mathbf{a}_{k,\text{MMSE}}^H = \frac{\mathbf{h}_k^H \mathbf{R}_k}{\mathbf{h}_k^H \mathbf{R}_k \mathbf{h}_k},$$

$$\mathbf{R}_k = \mathbf{I}_M - \bar{\mathbf{H}}_k \left(\frac{\sigma^2}{p} \mathbf{I}_{K-1} + \bar{\mathbf{H}}_k^H \bar{\mathbf{H}}_k \right)^{-1} \bar{\mathbf{H}}_k^H. \quad (37)$$

Based on the detected symbol $\hat{x}_k = \mathbf{a}_{k,\text{C}}^H \mathbf{y}$, $\text{C} \in \{\text{MRC}, \text{ZF}, \text{MMSE}\}$, the sum user rate is given by $R = \sum_{k=1}^K \log(1 + \text{SINR}_{k,\text{C}})$, where the SINR of user k is expressed as

$$\text{SINR}_{k,\text{MRC}} = \frac{p \|\mathbf{h}_k\|^2}{p \sum_{i=1, i \neq k}^K |\mathbf{h}_k^H \mathbf{h}_i|^2 / \|\mathbf{h}_k\|^2 + \sigma^2}, \quad (38)$$

$$\text{SINR}_{k,\text{ZF}} = \frac{p}{\sigma^2} \mathbf{h}_k^H \mathbf{P}_k \mathbf{h}_k, \quad (39)$$

$$\text{SINR}_{k,\text{MMSE}} = \frac{p}{\sigma^2} \mathbf{h}_k^H \mathbf{R}_k \mathbf{h}_k. \quad (40)$$

For conventional massive MIMO systems employing a ULA array [46], the far-field channel of user k can be expressed as $\mathbf{h}_k^{\text{far}} = \xi_k \left[1, e^{-j2\pi \frac{\Delta x}{\lambda} \sin \psi_k}, \dots, e^{-j2\pi \frac{\Delta x}{\lambda} (M-1) \sin \psi_k} \right]^T$. As can be seen, unlike the considered near-field channel model (3), the amplitudes of different entries of $\mathbf{h}_k^{\text{far}}$ are uniform and the phases of different entries of $\mathbf{h}_k^{\text{far}}$ are linearly scaled. Accordingly, the multi-user interference term in (38) can be calculated as [2], [46], [50]

$$\frac{|(\mathbf{h}_k^{\text{far}})^H \mathbf{h}_i^{\text{far}}|^2}{\|\mathbf{h}_k^{\text{far}}\|^2} = \frac{\sin^2 \left(\pi \frac{\Delta x}{\lambda} M (\sin \psi_i - \sin \psi_k) \right)}{M \sin^2 \left(\pi \frac{\Delta x}{\lambda} (\sin \psi_i - \sin \psi_k) \right)}. \quad (41)$$

Clearly, if user k and user i do not have the same angle, the interference will tend to zero as $M \rightarrow \infty$. Therefore, MRC detectors can achieve rather good performance. However, this favorable property no longer holds for near-field channels characterized by spherical wavefronts, where the amplitudes of different entries of \mathbf{h}_k are different and the phases are no longer linearly scaled either, as shown in (3). As a result, we have

$$\mathbf{h}_k^H \mathbf{h}_i = \sum_{m_x \in \mathcal{M}_x} \sum_{m_y \in \mathcal{M}_y} \sqrt{\xi_{k,m_x,m_y}^H \xi_{i,m_x,m_y}} e^{j \frac{2\pi}{\lambda} (r_{k,m_x,m_y} - r_{i,m_x,m_y})}, \quad (42)$$

which cannot be simplified as a function of the difference of the angles between users k and i . Meanwhile, the denominator term $\|\mathbf{h}_k\|^2$ remains finite for large M and therefore the fraction $|\mathbf{h}_k^H \mathbf{h}_i|^2 / \|\mathbf{h}_k\|^2$ does not tend to zero even if $M \rightarrow \infty$. This implies that the low-complexity MRC detector does not work well in XL-MIMO systems in the near field due to the severe interference. To eliminate the interference,

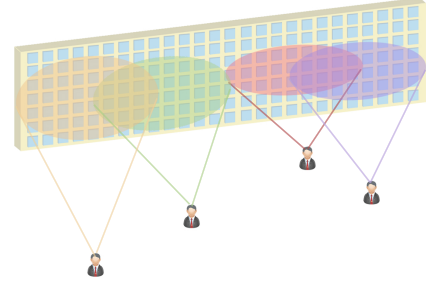


Fig. 4. Illustration of VRs for different users.

ZF or MMSE detectors are necessary, which significantly increases the computational complexity due to the required matrix inversion. To tackle this challenge, in the following, we propose low-complexity ZF/MMSE schemes by exploiting the near-field spatial non-stationarity.

B. VR-Based Low-Complexity Design

Section III has analytically shown that due to the amplitude attenuation across the array, the SNR is limited even for an infinitely large array. In other words, a limited part of the array receives a large portion of the signal power, which is referred to as the VR of the user, as illustrated in Fig. 4. The VR can be approximated as a combination of sub-arrays of the XL-MIMO array. Considering that the dimensions of the sub-arrays located within the VR of a user could be considerably smaller than the entire array, especially for large M , we can utilize the VR of each user to design low-complexity detectors for XL-MIMO.

Lemma 1 Assume that the XL-MIMO is partitioned into $S = S_x \times S_y$ sub-arrays. For the (s_x, s_y) -th sub-array, where $0 \leq s_x \leq S_x$ and $0 \leq s_y \leq S_y$, the power of signal received from user k is given by

$$P_{k,s_x,s_y} = \frac{p}{\sigma^2} \frac{\eta}{6\pi} \left\{ F_k(f_{s,y,1} \Delta_y - u_{k,y}, f_{s,x,1} \Delta_x - u_{k,x}) \right. \\ \left. + F_k(-f_{s,y,1} \Delta_y + u_{k,y}, f_{s,x,2} \Delta_x - u_{k,x}) \right. \\ \left. + F_k(-f_{s,y,2} \Delta_y + u_{k,y}, f_{s,x,1} \Delta_x - u_{k,x}) \right. \\ \left. + F_k(f_{s,y,2} \Delta_y - u_{k,y}, f_{s,x,2} \Delta_x - u_{k,x}) \right\}, \quad (43)$$

where $f_{s,c,1} = -\frac{M_c}{2} + s_c \frac{M_c}{S_c}$, $f_{s,c,2} = -\frac{M_c}{2} + (s_c + 1) \frac{M_c}{S_c}$, $c \in \{x, y\}$.

Proof: For the (s_x, s_y) -th subarray, we can obtain the indices of the antennas as $m_c \in \left\{ -\frac{(M_c-1)}{2} + s_c \frac{M_c}{S_c}, \dots, -\frac{(M_c-1)}{2} + (s_c + 1) \frac{M_c}{S_c} - 1 \right\}$, $c \in \{x, y\}$. The proof follows by deriving the sum of the powers across this sub-array using a similar method as in Appendix A. ■

Based on Lemma 1, the VR of user k can be determined by selecting the sub-arrays contributing to the main portion of the received SNR as ϖSNR_k , where $\varpi \in [0, 1]$ and SNR_k is given in (12). The procedure for detecting VR is outlined in Algorithm 1, where step 5 collects the sub-array indices for user k in set \mathcal{B}_k . Then, we can use only the sub-arrays

Algorithm 1 VR Detection

Input: ϖ , $\hat{P}_k = 0$, $\mathcal{B}_k = \emptyset$, SNR_k , $\mathcal{P}_k = \{P_{k,s_x,s_y}, \forall s_x, s_y\}$
Output: \mathcal{B}_k

- 1: **for** $k = 1 : K$ **do**
- 2: Sort \mathcal{P}_k using quicksort algorithms; $i = 1$;
- 3: **while** $\hat{P}_k \leq \varpi \text{SNR}_k$ **do**
- 4: Select the i -th element in \mathcal{P}_k referred to as P_{k,s_x^*,s_y^*} ;
- 5: $\mathcal{B}_k = \{\mathcal{B}_k \cup (s_y^* S_x + s_x^*)\}$;
- 6: $\hat{P}_k = \hat{P}_k + P_{k,s_x^*,s_y^*}$; $i = i + 1$;
- 7: **end while**
- 8: **end for**

belonging to \mathcal{B}_k to detect the symbol of user k , $\forall k$, which helps reduce the computational complexity. Specifically, for user k , we first construct the channel $\mathbf{H}_{\mathcal{B}_k} \in \mathcal{C}^{(\frac{|\mathcal{B}_k|}{S}M) \times K}$ from the K users to the antenna elements belonging to \mathcal{B}_k . Then, the symbol of user k can be detected based on the linear detectors in (38)-(40) by substituting the WA channel matrix \mathbf{H} with VR channel matrix $\mathbf{H}_{\mathcal{B}_k}$. Taking VR-based ZF as an example, we have $\mathbf{h}_k^{\text{VR}} = [\mathbf{H}_{\mathcal{B}_k}]_{(:,k)}$, $\bar{\mathbf{H}}_k^{\text{VR}} = [\mathbf{H}_{\mathcal{B}_k}]_{(:,mathcal{K} \setminus k)}$, and the detector of user k is obtained as

$$(\mathbf{a}_{k,\text{ZF}}^{\text{VR}})^H = \frac{(\mathbf{h}_k^{\text{VR}})^H \mathbf{P}_k^{\text{VR}}}{(\mathbf{h}_k^{\text{VR}})^H \mathbf{P}_k^{\text{VR}} \mathbf{h}_k^{\text{VR}}}, \quad (44)$$

where $\mathbf{P}_k^{\text{VR}} = \mathbf{I}_{\frac{|\mathcal{B}_k|}{S}M} - \bar{\mathbf{H}}_k^{\text{VR}} \left((\bar{\mathbf{H}}_k^{\text{VR}})^H \bar{\mathbf{H}}_k^{\text{VR}} \right)^{-1} (\bar{\mathbf{H}}_k^{\text{VR}})^H$.

C. User Partition-Based PZF

Next, we fully exploit the properties of the VRs to further reduce the computational complexity. In the near field, users located at different positions may have different VRs, and users whose VRs do not significantly overlap may suffer from low mutual interference. Therefore, we can partition the K users into several groups, where the VRs of users in different groups have low overlap. Then, the users will be mainly affected by the interference caused by the users in their own group. The interference from users in other groups is expected to be weak and can be neglected during detector design. As a result, we propose to utilize the PZF detector [51], [52], which eliminates only intra-group interference and therefore effectively reduces the computational complexity of the required matrix inversion. To begin with, we exploit the VR information to propose a user partition algorithm grounded in graph theory.

Definition 1 [53]: A undirected graph can be denoted as $G = (V, E)$, where V and E are the sets of vertices and edges, respectively. $(u, v) \in E$ means that there is an edge between vertices u and v . The neighborhood of u is $N(u) = \{v \in V | (u, v) \in E\}$ and the degree of u is $d(u) = |N(u)|$. A path D of G is a degree-two path if all vertices of D have edges with each other and have degree two. The maximum independent set of graph G is the maximum vertex set $\mathcal{I} \subseteq V$, in which all vertices have no edge.

Following Definition 1, we construct an undirected graph $G = (V, E)$ with $V = \{v_1, \dots, v_K\}$ corresponding to the

TABLE I
COMPUTATIONAL COMPLEXITY

WA_ZF	$\mathcal{O}\{M^2 K^2 + K^4\}$
VR_ZF	$\mathcal{O}\{(\tilde{\mathcal{B}} /S)^2 M^2 K^2 + K^4 + KS \log(S)\}$
UP_PZF	$\mathcal{O}\{(\tilde{\mathcal{B}} /S)^2 M^2 K^2 / \tilde{\mathcal{I}} + K^4 / \tilde{\mathcal{I}} ^3 + KS \log(S)\}$

K users. The edge (v_k, v_i) signifies the VR overlap situation between users k and i . Specifically, define $\hat{s}_{\text{ovp}} \in [0, 1]$ as a threshold specifying the maximum acceptable overlap ratio between the VRs of two users. If $\frac{|\mathcal{B}_k \cap \mathcal{B}_i|}{\min\{|\mathcal{B}_k|, |\mathcal{B}_i|\}} \geq \hat{s}_{\text{ovp}}$, the VR overlap ratio between users k and i exceeds the threshold, and we establish an edge $(v_k, v_i) \in E$. In order to reduce the matrix inversion complexity while guaranteeing the performance, our target is to partition users into as many as groups possible, where the VRs of different groups have low overlap. To this end, based on the graph $G = (V, E)$, we address the following maximum independent set problem:

$$\max |\mathcal{I}|, \text{ s.t. } \mathcal{I} \subseteq V; (u, v) \notin E, \forall u, v \in \mathcal{I}. \quad (45)$$

Upon solving the maximum independent set problem in (45), we obtain as many as possible vertices in G without edges between each other. In other words, we find as many as possible users with low-overlap VRs. Then, each vertex in \mathcal{I} and its neighborhood constitute a user group. Based on the user partitioning results, we design the PZF detector to eliminate only the intra-group interference. The detailed procedure is outlined in Algorithm 2. Specifically, steps 2 and 3 construct the graph G based on the VRs. Steps 4-14 find the maximum independent set \mathcal{I} of G exploiting a degree-based reduction algorithm with linear complexity $\mathcal{O}(K)$ [53]. Then, each vertex in \mathcal{I} with its neighborhood vertices form one user group \mathcal{L} . For each user group, steps 15-19 design the PZF detector by eliminating the interference within the group.

D. Complexity Analysis

For brevity, only the complexity of ZF is analyzed since MMSE and ZF have the same asymptotic complexity. We refer to the three algorithms as whole array-based ZF (WA_LD), VR-based ZF (VR_LD), and user partitioning-based PZF (UP_PZF). The results are presented in Table I. For tractability, we consider an ideal scenario where the VR of each user includes the same number of sub-arrays, i.e., $|\mathcal{B}_k| = |\tilde{\mathcal{B}}|$, $\forall k$. Then, the number of antennas in the VR of each user reduces from M to $\frac{|\tilde{\mathcal{B}}|}{S}M$. We also ideally assume that for the user partitioning algorithm, K users are divided uniformly into $|\tilde{\mathcal{I}}|$ groups. Therefore, the matrix dimension for the inversion operation in the PZF scheme diminishes from K to $K/|\tilde{\mathcal{I}}|$. Table I reveals that the proposed algorithms can significantly reduce the complexity when $|\tilde{\mathcal{B}}|/S$ is small and when $|\tilde{\mathcal{I}}|$ is large.

V. NUMERICAL RESULTS

In this section, we provide numerical results for validating our analytical conclusions and providing insight into the

Algorithm 2 User Partition-Based PZF

- 1: Initialize $\mathcal{I} = \emptyset$
 - 2: Construct graph $G = (V, E)$, $V = \{v_1, \dots, v_K\}$, $(v_k, v_i) \in E$ if $|\mathcal{B}_k \cap \mathcal{B}_i| \geq \hat{s}_{\text{ovp}} \min\{|\mathcal{B}_k|, |\mathcal{B}_i|\}$
 - 3: Calculate degree $d(v_k)$, $\forall k$; $\mathcal{V}_1 = \{v_k | d(v_k) = 1, \forall k\}$, $\mathcal{V}_2 = \{v_k | d(v_k) = 2, \forall k\}$, $\mathcal{V}_3 = \{v_k | d(v_k) > 2, \forall k\}$
 - 4: **while** \mathcal{V}_1 or \mathcal{V}_2 or $\mathcal{V}_3 \neq \emptyset$ **do**
 - 5: **if** $\mathcal{V}_1 \neq \emptyset$ **then**
 - 6: Delete the neighborhood of $v_k \in \mathcal{V}_1$ from G
 - 7: **else if** $\mathcal{V}_2 \neq \emptyset$ **then**
 - 8: Select a vertex $v_k \in \mathcal{V}_2$, find its maximal degree-two path, and delete vertices based on rules in [53, Lemma 4.1]
 - 9: **else**
 - 10: Delete the vertex with the largest degree
 - 11: **end if**
 - 12: Update the degree for all vertices
 - 13: **end while**
 - 14: $\mathcal{I} = \{v_k | d(v_k) = 0, \forall k\}$
 - 15: **while** $\mathcal{I} \neq \emptyset$ **do**
 - 16: Select $u \in \mathcal{I}$; construct $\mathcal{L} = \{i | v_i \in \{u, N(u)\} \cap i \in \mathcal{K}\}$
 - 17: For users i , $i \in \mathcal{L}$, design $\mathbf{a}_{i, \text{PZF}}^H = \frac{\hat{\mathbf{h}}_i^H \mathbf{L}_i}{\hat{\mathbf{h}}_i^H \mathbf{L}_i \hat{\mathbf{h}}_i}$, $\mathbf{L}_i = \mathbf{I}_{|\mathcal{B}_i| \frac{M}{S}} - \hat{\mathbf{H}}_{\mathcal{L} \setminus i} \left(\hat{\mathbf{H}}_{\mathcal{L} \setminus i}^H \hat{\mathbf{H}}_{\mathcal{L} \setminus i} \right)^{-1} \hat{\mathbf{H}}_{\mathcal{L} \setminus i}^H$, where $\hat{\mathbf{H}}_{\mathcal{L} \setminus i} = \mathbf{H}(\mathcal{M}_i^{\text{VR}}, \mathcal{L} \setminus i)$, $\hat{\mathbf{h}}_i = \mathbf{H}(\mathcal{M}_i^{\text{VR}}, i)$, and $\mathcal{M}_i^{\text{VR}}$ denotes the antennas indices in the VR of user i
 - 18: Remove u from \mathcal{I}
 - 19: **end while**
-

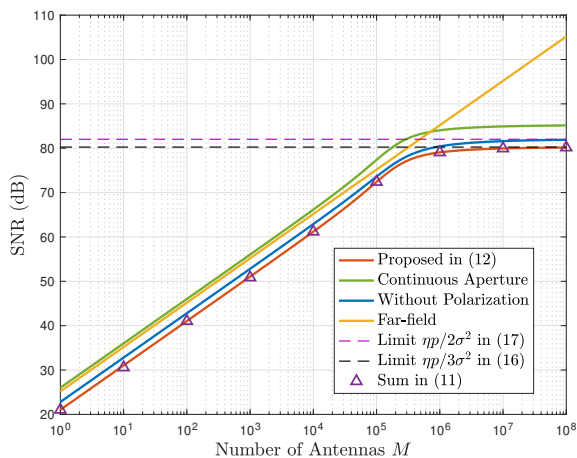


Fig. 5. SNR versus M for XL-UPA, $\mathbf{u}_k = [10, 10, 10]$, $M_x = M_y = \sqrt{M}$.

performance of XL-MIMO systems. Consistent with existing literature [30]–[33], we set $\Delta_x = \Delta_y = \frac{\lambda}{2} = 0.0628$ m, $\frac{p}{\sigma^2} = 90$ dB, and $A = \frac{\lambda^2}{4\pi}$.

A. Single-User Case

To begin with, the single-user case is considered. Fig. 5 depicts the SNR performance as the aperture of the XL-UPA grows infinitely large. It can be seen that unlike the far field-based result which increases linearly with M , the near

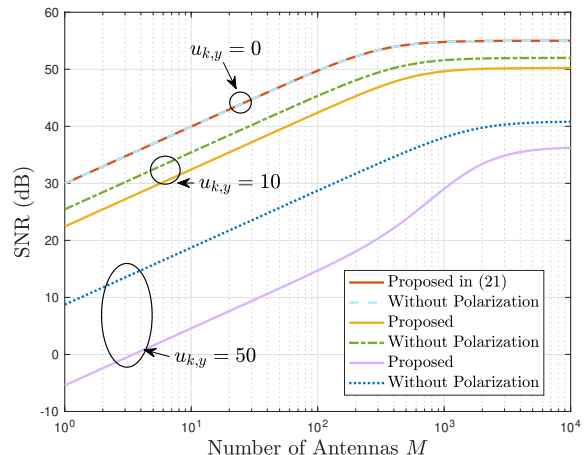


Fig. 6. SNR versus M for XL-ULA, $\mathbf{u}_k = [0, u_{k,y}, 10]$, $M_x = M$, $M_y = 1$.

field-based SNR initially increases but ultimately saturates as M approaches infinity. Furthermore, the proposed model, which takes into consideration both the discrete aperture and polarization mismatch, characterizes the actual performance with additional loss. Besides, it can be seen that the SNR in (11) which includes a double sum is well approximated by the derived explicit result.

In Fig. 6, the asymptotic SNR of XL-ULA is studied. A similar tendency as in Fig. 5 is observed. However, the number of antennas needed for the SNR growth rate to slow down is notably smaller than that in Fig. 5. The SNR of ULA attains saturation with roughly 10^3 antenna elements, whereas the required number of antenna elements for UPA is 10^6 . This is because given a value of M , the ULA has a considerably larger dimension than the UPA. Consequently, the variations in amplitudes, angles between the signal incident direction and the array normal, and polarization mismatch become more pronounced across the whole array. As a result, the near-field behavior becomes more obvious for the ULA with a given M . This phenomenon can also be understood via the geometric figures in Figs. 2 and 3. As M increases, the enlarging of view of angles γ is easier to saturate for the ULA than angles α and β for the UPA. Furthermore, it can be observed that the SNR gap between the proposed EM model and the model without polarization mismatch enlarges as the y -coordinate of the user increases. This phenomenon agrees with our analytical result (24) since the polarization mismatch is proportional to the difference in the y -coordinate between the user and the received antenna. As a result, as $u_{k,y}$ increases, the performance loss caused by polarization mismatch increases, which enlarges the gap.

Fig. 7 illustrates the proposed near-/far-field boundaries on the plane of $u_{k,y} = 0$ ($\psi_k^a = 0$ or π). The threshold \bar{v}_t is chosen to be 0.9 or 0.95 so that the power difference across the whole array can be neglected in the far field. It can be seen that the phase-based boundary considering different signal incident directions is smaller than the classical Fraunhofer distance, and it keeps shrinking as ψ_k^e increases from 0 to $\pi/2$, which is consistent with our analysis below (30). Besides, it can be seen

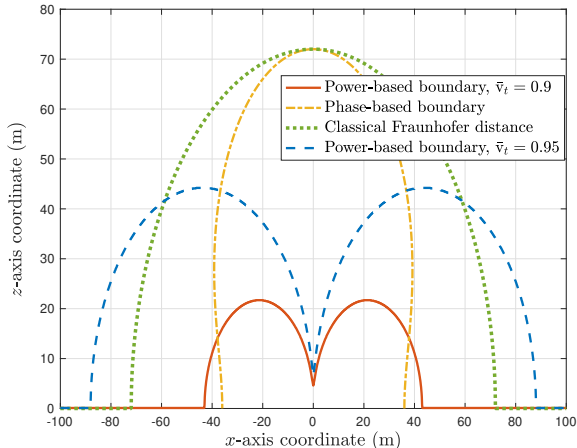


Fig. 7. Field boundaries at $u_{k,y} = 0$, $M_x = M_y = 25$.

that the signal power-based boundary has a different shape from the phase-based boundary. It shrinks as the user moves towards the center of the array (i.e., as x -coordinate $\rightarrow 0$). This is because the variation of the power from the center to the edge of the array is smaller than that from one edge to the other edge of the array. For a milder amplitude variation, the near-field region is reduced. Furthermore, the signal power-based boundary expands with \bar{v}_t due to the stricter requirement of the degree of the power variation across the array for the far field. Combining the power and phase-based boundaries can provide a useful reference for the practical algorithm design of the XL-MIMO.

B. Multi-User Case

The previous subsection illustrated the impact of near-field spatial non-stationarities, which inspired the proposed low-complexity design for multi-user scenarios. In this section, numerical results are presented to illustrate the effectiveness of the proposed algorithms. Unless stated otherwise, we assume that $M = 10^4$, $M_y = 10$, $S_y = 2$, $M_x/S_x = 10$, $\varpi = 0.8$, and $\hat{s}_{\text{ovp}} = 0.6$. $K = 20$ users are randomly distributed within the region of $[-25, 25] \times [2, 12]$ on the xoz plane.

In Fig. 8, we compare the performance of the whole array (WA)-based design with the proposed VR-based design. The WA-based MMSE, ZF, and MRC detection are carried out based on (35)-(37), while the VR-based design is conducted as (44). It can be seen that for both the WA and VR-based cases, the sum user rates for the MMSE and ZF detectors coincide for large M and are much higher than that for MRC. This is because in near-field scenarios with spherical wavefronts, the favorable interference condition in (41) no longer holds, which deteriorates to (42) as a function of distances and angles. Therefore, considering that the computational complexity of ZF and MMSE is much higher than that of MRC, it is necessary to employ low-complexity detectors in XL-MIMO systems. From Fig. 8, it can be observed that the proposed VR-based low-complexity MMSE and ZF detectors perform very close to the WA-based design, especially for large M . This is because for XL-MIMO with large physical dimensions, the

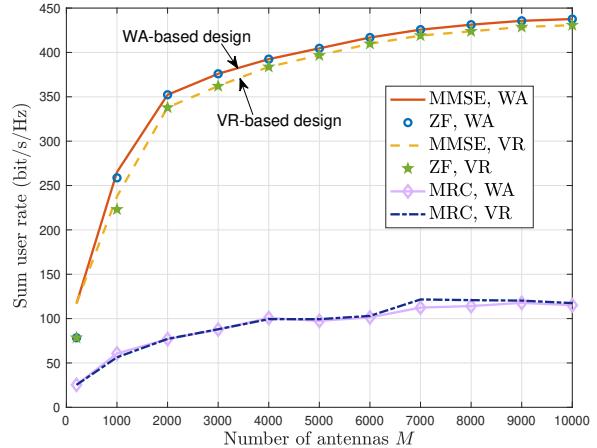


Fig. 8. Comparison of WA and VR-based designs.

variations in amplitudes, angles between the signal incident directions and array normal, and polarization mismatch are pronounced across the whole array. As a result, the majority of the signal power is received on a limited portion of the array. In other words, the user will “see” only a part of the array (i.e., the VR). If the VRs are accurately detected, it is expected that the proposed VR-based algorithms can achieve performance comparable to that of the WA-based design. Meanwhile, for large M , the portion of the array that contributes marginal received power grows. Thus, for a given ratio ϖ , the VR detection algorithm (Algorithm 1) is more efficient in finding the most relevant sub-arrays, thus diminishing the performance gap between the VR and WA-based designs.

Intuitively, the proposed VR-based design aims to achieve a trade-off between performance and complexity, which can be adjusted by the VR detection ratio ϖ as shown in Algorithm 1. To quantify the complexity, the ratio of the average number of antennas employed by the VR-based design to the number of antennas employed by the WA-based design is defined as $r_{oc} = \frac{1}{K} \sum_{k \in \mathcal{K}} \frac{|\mathcal{B}_k|}{S}$. Clearly, we have $r_{oc} = 1$ for the WA-based design. Next, Figs. 9 and 10 illustrate the trade-off between performance and complexity when utilizing VR-based detectors.

In Fig. 9, we observe that ratio r_{oc} is an increasing function of the VR detection ratio ϖ , which implies that the number of antennas considered for the computation of VR-based detectors increases with ϖ . This is because the VR is defined as the set of sub-arrays that contribute a fraction of ϖ to the total received power. The larger ϖ is, the more sub-arrays are included in the VR. Besides, as can be seen, r_{oc} is a decreasing function of M . For small M , r_{oc} can even approach 1. This phenomenon actually underscores the rationale behind introducing the VR-based design for XL-MIMO. Specifically, as the number of antennas increases, the physical dimensions of the array also grow, and the portion of the array that receives marginal power increases. In this context, it is inefficient to use the whole array to compute the symbol detectors, since the majority of the power concentrates in a small portion of the array. Conversely, when M is small, all sub-arrays may

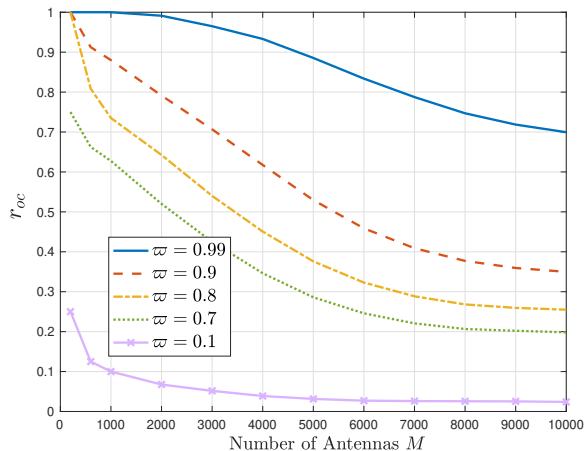


Fig. 9. Ratio of average number of antennas employed by VR-based design.

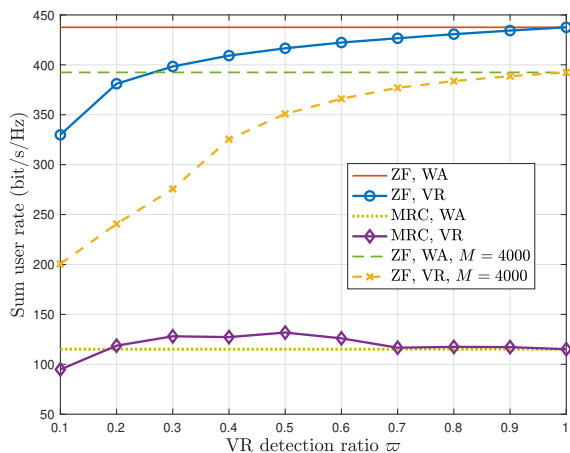


Fig. 10. Sum user rate under different ϖ , where $M = 10^4$.

receive non-negligible power and therefore r_{oc} approaches one. It can be seen from Fig. 9 that for an XL-MIMO array with $M = 10^4$, 25% of the antennas receive 80% of the total power (i.e., $\varpi = 0.8$), which can be harnessed to substantially curtail the computational complexity in VR-based detection.

Fig. 10 reveals the performance loss caused by the reduction of the complexity. As can be seen, when using ZF detection, the performance loss is small for moderate values of ϖ , whereas performance deteriorates when ϖ is small. This is because as shown in Fig. 9, when $M = 10^4$, less than 5% of the antennas contribute 10% of the power, 20% of the antennas contribute 70% of the power, and 70% of the antennas contribute 99% of the power. As a result, for a moderate value of ϖ , it is feasible to identify sub-arrays that receive the dominant power within the VR while encompassing a small number of antennas, which yields good performance at low complexity. In other words, a moderate value of ϖ can realize a good trade-off between performance and complexity. Besides, it can be observed that when ϖ is small, the data rate degradation is severer under smaller M . This is because smaller arrays exhibit weaker spatial non-stationarity effects, and therefore more sub-arrays have to be used to receive sufficient power

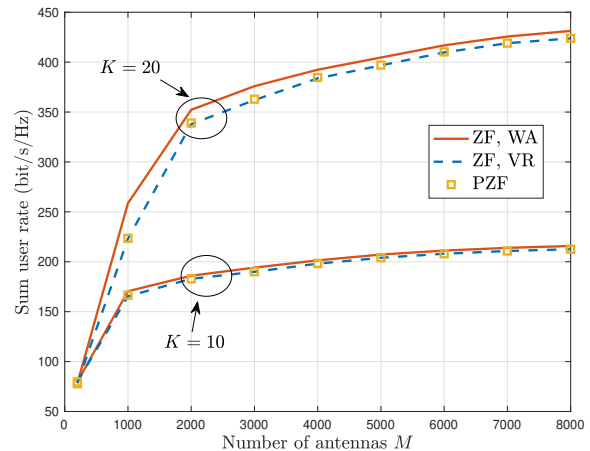


Fig. 11. Comparison of VR-based and PZF-based design, $\varpi = 0.8$, $\hat{\delta}_{ovp} = 0.6$.

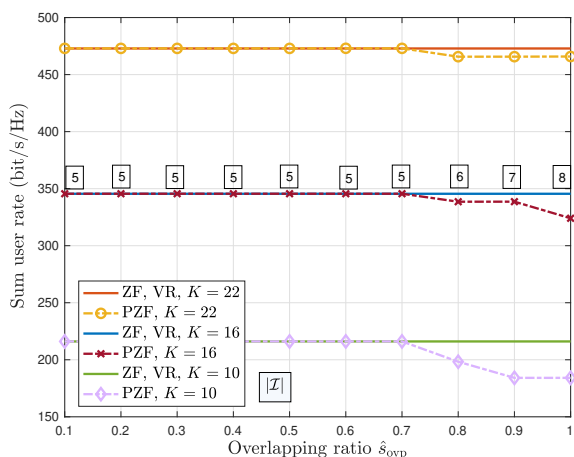


Fig. 12. Sum user rate versus the threshold of VR overlapping ratio $\hat{\delta}_{ovp}$.

and attain satisfactory performance. Furthermore, for MRC, the VR-based design may outperform the WA-based design. The reason is that for VR-based MRC, the influence of multi-user interference diminishes when the VRs of users have less overlap.

In Figs. 11 and 12, we investigate the performance of the proposed user partitioning-based PZF algorithm. Fig. 11 shows that the proposed PZF detector can achieve almost the same performance as the VR-based detectors for any value of M and for different values of K . This is because for the VR-based detectors, users primarily suffer from the interference from other users having VRs with large overlap. Therefore, it is reasonable to partition users into different groups based on VR information, and then eliminate only the intra-group interference. Meanwhile, for the PZF detectors, a part of the channel degrees-of-freedom (DoFs) are used for interference nulling while the remaining DoFs are used to enhance the desired signal, which is beneficial for performance improvement.

The PZF detectors exploit user partitioning which is determined by VR overlap threshold $\hat{\delta}_{ovp}$, as specified in Algorithm

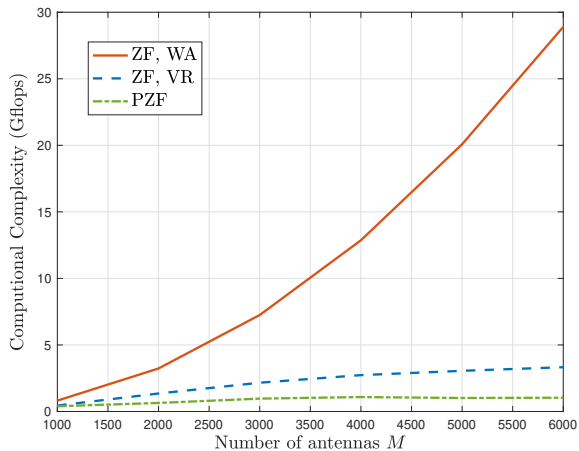


Fig. 13. Comparison of the computational complexity.

2. In Fig. 12, we observe that the PZF algorithm only causes a performance loss for large \hat{s}_{ovp} . This is because as \hat{s}_{ovp} increases, the criterion for establishing an edge between two vertices becomes more stringent, and thus the size of the independent set $|Z|$ could grow. In other words, for large \hat{s}_{ovp} , users significantly interfering with each other may not be connected by edges, and they could be partitioned into different groups, and therefore the dominant interference may not be eliminated clearly by the intra-group PZF algorithm. With proper user partitioning (moderate \hat{s}_{ovp}), the PZF algorithm can effectively address predominant interference and therefore cause negligible performance loss at low complexity.

Fig. 13 shows the computational complexity associated with WA-based ZF, VR-based ZF, and user partitioning-based PZF detection. In accordance with Table I, the complexity is computed based on the actual VR detection and user partitioning results utilizing MATLAB. As can be seen, the complexity of the conventional WA-based design has a polynomial growth rate, which is not favorable considering the large number of antennas typically for XL-MIMO systems. However, by effectively exploiting the near-field spatial non-stationarities, the two proposed algorithms achieve much lower complexities. VR-based ZF detection has a complexity that increases sub-linearly with the number of antennas, and the complexity of user partitioning-based PZF practically saturates for large M . The rationale behind this trend is twofold. On the one hand, the growth rate of the number of antennas within VRs is considerably lower than M . As shown in Fig. 9, given $\varpi = 0.7$, as M increases from 10^3 to 10^4 , the average number of antennas within VRs only increases from 600 to 2000. On the other hand, for large M , the physical dimensions of the array expand, and therefore, the VRs of different users become more separated on average. Accordingly, users can be divided into more groups, and then the computational complexity needed for PZF to eliminate the intra-group interference reduces.

Finally, Fig. 14 illustrates the motivation and benefits of employing XL-MIMO. It can be seen that XL-MIMO has the capability to support a large number of users with extremely high throughput. As the number of users K grows, small gaps

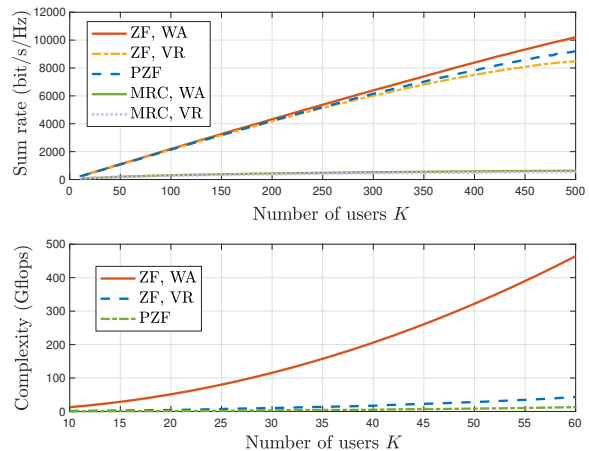


Fig. 14. Sum user rate versus the number of users, $\varpi = 0.8$.

emerge between the proposed low-complexity designs and the WA-based design. This is because the property of the multi-user interference becomes more and more complicated as K increases. Nevertheless, the gaps can be effectively narrowed by increasing the value of ϖ . Meanwhile, it is shown that as K increases, the proposed algorithms exhibit significantly lower computational complexity. Therefore, the proposed VR-based and user partitioning-based PZF algorithms can effectively support extremely-high capacities in XL-MIMO systems at comparatively low complexity. Fig. 14 also confirms the effectiveness and necessity of exploiting spatial non-stationarities when using the XL-MIMO.

VI. CONCLUSION

In this work, we investigated the performance characteristics of XL-MIMO systems based on the EM channel model with near-field spatial non-stationarities. We derived an explicit expression for the SNR for the single-user scenario, which provided useful insights into the impact of the discrete aperture and polarization mismatch. We also complemented the classical Fraunhofer distance under the proposed EM channel model. Building upon the near-field characteristics, we introduced a novel low-complexity linear detector based on VR information. We also proposed a user partitioning algorithm grounded in graph theory, based on which PZF was used to further reduce the computational complexity. Simulation results validated the effectiveness of the proposed two low-complexity algorithms.

APPENDIX A

Define $\epsilon_x = \frac{\Delta_x}{r_{k,o}}$ and $\epsilon_y = \frac{\Delta_y}{r_{k,o}}$, where $r_{k,o} = \|\mathbf{u}_k\|$ is the distance between user k and the origin. Substituting ξ_{k,m_x,m_y}

in (11) with (9), we have

$$\text{SNR}_k = \frac{p}{\sigma^2} \sum_{m_y \in \mathcal{M}_y} \sum_{m_x \in \mathcal{M}_x} \frac{A}{4\pi} \frac{u_{k,z} \left((m_x \Delta_x - u_{k,x})^2 + u_{k,z}^2 \right)}{\left\{ (m_x \Delta_x - u_{k,x})^2 + (m_y \Delta_y - u_{k,y})^2 + u_{k,z}^2 \right\}^{\frac{5}{2}}} \quad (46)$$

$$= \frac{p}{\sigma^2} \sum_{m_y \in \mathcal{M}_y} \sum_{m_x \in \mathcal{M}_x} \frac{\eta \epsilon_x \epsilon_y}{4\pi} \frac{\bar{u}_{k,z} \left((m_x \epsilon_x - \bar{u}_{k,x})^2 + \bar{u}_{k,z}^2 \right)}{\left\{ (m_x \epsilon_x - \bar{u}_{k,x})^2 + (m_y \epsilon_y - \bar{u}_{k,y})^2 + \bar{u}_{k,z}^2 \right\}^{\frac{5}{2}}}, \quad (47)$$

where $\bar{u}_{k,c} = \frac{u_{k,c}}{r_{k,o}}$, $c \in \{x, y, z\}$. Since $r_{k,o} \gg \Delta_x, \Delta_y$, we have $\epsilon_x, \epsilon_y \ll 1$. Then, we obtain (48) shown at the bottom of the page, where the change of variables $\hat{x} = m_x \epsilon_x$ and $\hat{y} = m_y \epsilon_y$ is applied in (a). In (b), since $\epsilon_x, \epsilon_y \ll 1$, all variables within domain $[\hat{x} \pm \frac{\epsilon_x}{2}] \times [\hat{y} \pm \frac{\epsilon_y}{2}]$ of area $\epsilon_x \epsilon_y$ approximately yield the same objective function value as the center point (\hat{x}, \hat{y}) . Then, the double sum is approximated by a double integral divided by $\frac{1}{\epsilon_x \epsilon_y}$. The change of variables $x = \hat{x} - \bar{u}_{k,x}$ and $y = \hat{y} - \bar{u}_{k,y}$ are used in (c). The proof can be completed by first solving the integral with respect to y based on [54, 2.271.6] and then solving the integral with respect to x using [54, (2.271.5)] and [54, (2.284)].

APPENDIX B

For the case of $M_y = 1$, we obtain (49), shown at the bottom of the page. Utilizing [54, (2.271.5)] and [54, (2.271.6)], we can complete the proof after some algebraic operations.

REFERENCES

- [1] K. Zhi, C. Pan, T. Wu, H. Ren, and K. K. Chai, "Analysis of XL-array with near-field EM channels," accepted by the 30th European Signal Processing Conference (EUSIPCO), Helsinki, Finland, 2023.
- [2] E. Björnson, J. Hoydis, and L. Sanguinetti, "Massive MIMO networks: Spectral, energy, and hardware efficiency," *Found. Trends Signal Process.*, vol. 11, no. 3-4, pp. 154–655, Nov. 2017.
- [3] E. Björnson, M. Matthaiou, and M. Debbah, "Massive MIMO with non-ideal arbitrary arrays: Hardware scaling laws and circuit-aware design," *IEEE Trans. Wireless Commun.*, vol. 14, no. 8, pp. 4353–4368, Aug. 2015.
- [4] J. Zhang, E. Björnson, M. Matthaiou, D. W. K. Ng, H. Yang, and D. J. Love, "Prospective multiple antenna technologies for beyond 5G," *IEEE J. Sel. Areas Commun.*, vol. 38, no. 8, pp. 1637–1660, Aug. 2020.
- [5] K. Zhi, C. Pan, G. Zhou, H. Ren, M. El-kashlan, and R. Schober, "Is RIS-aided massive MIMO promising with ZF detectors and imperfect CSI?" *IEEE J. Sel. Areas Commun.*, vol. 40, no. 10, pp. 3010–3026, Oct. 2022.
- [6] E. Björnson and L. Sanguinetti, "Scalable cell-free massive MIMO systems," *IEEE Trans. Communications*, vol. 68, no. 7, pp. 4247–4261, Jul. 2020.
- [7] G. Chen, L. Qiu, and Y. Li, "Stochastic geometry analysis of coordinated beamforming small cell networks with CSI delay," *IEEE Commun. Lett.*, vol. 22, no. 5, pp. 1066–1069, May 2018.
- [8] R. W. Heath, N. González-Prelcic, S. Rangan, W. Roh, and A. M. Sayeed, "An overview of signal processing techniques for millimeter wave MIMO systems," *IEEE J. Sel. Topics Signal Process.*, vol. 10, Apr. 2016.
- [9] C. Pan *et al.*, "Intelligent reflecting surface aided MIMO broadcasting for simultaneous wireless information and power transfer," *IEEE J. Sel. Areas Commun.*, vol. 38, no. 8, pp. 1719–1734, Aug. 2020.
- [10] C. Huang *et al.*, "Reconfigurable intelligent surfaces for energy efficiency in wireless communication," *IEEE Trans. Wireless Commun.*, vol. 18, no. 8, pp. 4157–4170, Aug. 2019.
- [11] C. Pan *et al.*, "Multicell MIMO communications relying on intelligent reflecting surfaces," *IEEE Trans. Wireless Commun.*, vol. 19, no. 8, pp. 5218–5233, Aug. 2020.
- [12] G. Chen, Q. Wu, C. He, W. Chen, J. Tang, and S. Jin, "Active IRS aided multiple access for energy-constrained IoT systems," *IEEE Trans. Wireless Commun.*, vol. 22, no. 3, pp. 1677–1694, Mar. 2023.
- [13] E. Björnson, L. Sanguinetti, H. Wymeersch, J. Hoydis, and T. L. Marzetta, "Massive MIMO is a reality—what is next?: Five promising

$$\begin{aligned} \text{SNR}_k &\stackrel{(a)}{=} \frac{p}{\sigma^2} \frac{\eta \epsilon_x \epsilon_y}{4\pi} \sum_{\hat{y} = \frac{-(M_y-1)\epsilon_y}{2}}^{\frac{(M_y-1)\epsilon_y}{2}} \sum_{\hat{x} = \frac{-(M_x-1)\epsilon_x}{2}}^{\frac{(M_x-1)\epsilon_x}{2}} \frac{\bar{u}_{k,z} \left((\hat{x} - \bar{u}_{k,x})^2 + \bar{u}_{k,z}^2 \right)}{\left\{ (\hat{x} - \bar{u}_{k,x})^2 + (\hat{y} - \bar{u}_{k,y})^2 + \bar{u}_{k,z}^2 \right\}^{\frac{5}{2}}} \\ &\stackrel{(b)}{\approx} \frac{p}{\sigma^2} \frac{\eta \epsilon_x \epsilon_y}{4\pi} \frac{1}{\epsilon_x \epsilon_y} \int_{\frac{-(M_y-1)\epsilon_y}{2} - \frac{\epsilon_y}{2}}^{\frac{(M_y-1)\epsilon_y}{2} + \frac{\epsilon_y}{2}} \int_{\frac{-(M_x-1)\epsilon_x}{2} - \frac{\epsilon_x}{2}}^{\frac{(M_x-1)\epsilon_x}{2} + \frac{\epsilon_x}{2}} \frac{\bar{u}_{k,z} \left((\hat{x} - \bar{u}_{k,x})^2 + \bar{u}_{k,z}^2 \right)}{\left\{ (\hat{x} - \bar{u}_{k,x})^2 + (\hat{y} - \bar{u}_{k,y})^2 + \bar{u}_{k,z}^2 \right\}^{\frac{5}{2}}} d\hat{x} d\hat{y} \\ &\stackrel{(c)}{=} \frac{p}{\sigma^2} \frac{\eta \bar{u}_{k,z}}{4\pi} \int_{\frac{-M_x \epsilon_x}{2} - \bar{u}_{k,x}}^{\frac{M_x \epsilon_x}{2} - \bar{u}_{k,x}} \int_{\frac{-M_y \epsilon_y}{2} - \bar{u}_{k,y}}^{\frac{M_y \epsilon_y}{2} - \bar{u}_{k,y}} \frac{(x^2 + \bar{u}_{k,z}^2)}{\left\{ x^2 + y^2 + \bar{u}_{k,z}^2 \right\}^{\frac{5}{2}}} dy dx, \end{aligned} \quad (48)$$

$$\begin{aligned} \text{SNR}_k &= \frac{p}{\sigma^2} \frac{\eta \epsilon_x \epsilon_y}{4\pi} \sum_{m_x = \frac{-(M_x-1)}{2}}^{\frac{(M_x-1)}{2}} \frac{\bar{u}_{k,z} \left((m_x \epsilon_x - \bar{u}_{k,x})^2 + \bar{u}_{k,z}^2 \right)}{\left\{ (m_x \epsilon_x - \bar{u}_{k,x})^2 + \bar{u}_{k,y}^2 + \bar{u}_{k,z}^2 \right\}^{\frac{5}{2}}} \approx \frac{p}{\sigma^2} \frac{\eta \epsilon_x \epsilon_y}{4\pi} \frac{1}{\epsilon_x} \int_{\frac{-M_x \epsilon_x}{2}}^{\frac{M_x \epsilon_x}{2}} \frac{\bar{u}_{k,z} \left((\hat{x} - \bar{u}_{k,x})^2 + \bar{u}_{k,z}^2 \right)}{\left\{ (\hat{x} - \bar{u}_{k,x})^2 + \bar{u}_{k,y}^2 + \bar{u}_{k,z}^2 \right\}^{\frac{5}{2}}} d\hat{x} \\ &= \frac{p}{\sigma^2} \frac{\eta \epsilon_y}{4\pi} \bar{u}_{k,z} \int_{\frac{-M_x \epsilon_x}{2} - \bar{u}_{k,x}}^{\frac{M_x \epsilon_x}{2} - \bar{u}_{k,x}} \frac{1}{\left\{ x^2 + \bar{u}_{k,y}^2 + \bar{u}_{k,z}^2 \right\}^{\frac{3}{2}}} - \frac{\bar{u}_{k,y}^2}{\left\{ x^2 + \bar{u}_{k,y}^2 + \bar{u}_{k,z}^2 \right\}^{\frac{5}{2}}} dx. \end{aligned} \quad (49)$$

- research directions for antenna arrays,” *Digital Signal Process.*, vol. 94, pp. 3–20, Nov. 2019.
- [14] Z. Wang, J. Zhang, H. Du, W. E. Sha, B. Ai, D. Niyato, and M. Debbah, “Extremely large-scale MIMO: Fundamentals, challenges, solutions, and future directions,” *arXiv preprint arXiv:2209.12131*, 2022.
- [15] E. De Carvalho, A. Ali, A. Amiri, M. Angelichinoski, and R. W. Heath, “Non-stationarities in extra-large-scale massive MIMO,” *IEEE Wireless Commun.*, vol. 27, no. 4, pp. 74–80, Aug. 2020.
- [16] K. T. Selvan and R. Janaswamy, “Fraunhofer and fresnel distances: Unified derivation for aperture antennas,” *IEEE Antennas Propag. Mag.*, vol. 59, no. 4, pp. 12–15, Aug. 2017.
- [17] M. Cui, L. Dai, Z. Wang, S. Zhou, and N. Ge, “Near-field rainbow: Wideband beam training for XL-MIMO,” *IEEE Trans. Wireless Commun.*, early access, 2022.
- [18] W. Liu, H. Ren, C. Pan, and J. Wang, “Deep learning based beam training for extremely large-scale massive MIMO in near-field domain,” *IEEE Commun. Lett.*, vol. 27, no. 1, pp. 170–174, Jan. 2023.
- [19] Y. Zhang, X. Wu, and C. You, “Fast near-field beam training for extremely large-scale array,” *IEEE Wireless Commun. Lett.*, vol. 11, no. 12, pp. 2625–2629, Dec. 2022.
- [20] M. Cui and L. Dai, “Channel estimation for extremely large-scale MIMO: Far-field or near-field?” *IEEE Trans. Commun.*, vol. 70, no. 4, pp. 2663–2677, Jan. 2022.
- [21] Z. Wu and L. Dai, “Multiple access for near-field communications: SDMA or LDMA?” *IEEE J. Sel. Areas Commun.*, vol. 41, no. 6, pp. 1918–1935, Jun. 2023.
- [22] S. Hu, F. Rusek, and O. Edfors, “Beyond massive MIMO: The potential of data transmission with large intelligent surfaces,” *IEEE Trans. Signal Process.*, vol. 66, no. 10, pp. 2746–2758, May 2018.
- [23] D. Dardari, “Communicating with large intelligent surfaces: Fundamental limits and models,” *IEEE J. Sel. Areas Commun.*, vol. 38, no. 11, pp. 2526–2537, Nov. 2020.
- [24] E. Björnson and L. Sanguinetti, “Power scaling laws and near-field behaviors of massive MIMO and intelligent reflecting surfaces,” *IEEE Open J. Commun. Soc.*, vol. 1, pp. 1306–1324, Sep. 2020.
- [25] A. de Jesus Torres, L. Sanguinetti, and E. Björnson, “Near-and far-field communications with large intelligent surfaces,” in *Proc. 54th Asilomar Conference on Signals, Systems, and Computers*, 2020, pp. 564–568.
- [26] E. Björnson, Ö. T. Demir, and L. Sanguinetti, “A primer on near-field beamforming for arrays and reconfigurable intelligent surfaces,” in *Proc. 55th Asilomar Conference on Signals, Systems, and Computers*, 2021, pp. 105–112.
- [27] A. Pizzo, L. Sanguinetti, and T. L. Marzetta, “Spatial characterization of electromagnetic random channels,” *IEEE Open J. Commun. Soc.*, vol. 3, pp. 847–866, May 2022.
- [28] L. Wei, C. Huang, G. C. Alexandropoulos, Z. Yang, J. Yang, W. E. Sha, M. Debbah, and C. Yuen, “Channel modeling and multi-user precoding for Tri-polarized holographic MIMO communications,” *arXiv preprint arXiv:2302.05337*, 2023.
- [29] N. Decarli and D. Dardari, “Communication modes with large intelligent surfaces in the near field,” *IEEE Access*, vol. 9, pp. 165 648–165 666, Dec. 2021.
- [30] H. Lu and Y. Zeng, “Communicating with extremely large-scale array/surface: Unified modelling and performance analysis,” *IEEE Trans. Wireless Commun.*, vol. 21, no. 6, pp. 4039–4053, Jun. 2021.
- [31] —, “Near-field modeling and performance analysis for multi-user extremely large-scale MIMO communication,” *IEEE Commun. Lett.*, vol. 26, no. 2, pp. 277–281, Feb. 2022.
- [32] X. Li, H. Lu, Y. Zeng, S. Jin, and R. Zhang, “Near-field modeling and performance analysis of modular extremely large-scale array communications,” *IEEE Commun. Lett.*, vol. 26, no. 7, pp. 1529–1533, Jul. 2022.
- [33] —, “Modular extremely large-scale array communication: Near-field modelling and performance analysis,” *China Commun.*, vol. 20, no. 4, pp. 132–152, Apr. 2023.
- [34] S. Payami and F. Tufvesson, “Channel measurements and analysis for very large array systems at 2.6 GHz,” in *Proc. 6th European Conference on Antennas and Propagation (EUCAP)*, 2012, pp. 433–437.
- [35] Y. Han, S. Jin, C.-K. Wen, and X. Ma, “Channel estimation for extremely large-scale massive MIMO systems,” *IEEE Wireless Commun. Lett.*, vol. 9, no. 5, pp. 633–637, May 2020.
- [36] X. Li, S. Zhou, E. Björnson, and J. Wang, “Capacity analysis for spatially non-wide sense stationary uplink massive MIMO systems,” *IEEE Trans. Wireless Commun.*, vol. 14, no. 12, pp. 7044–7056, Dec. 2015.
- [37] A. Ali, E. De Carvalho, and R. W. Heath, “Linear receivers in non-stationary massive MIMO channels with visibility regions,” *IEEE Wireless Commun. Lett.*, vol. 8, no. 3, pp. 885–888, Jun. 2019.
- [38] X. Yang, F. Cao, M. Matthaiou, and S. Jin, “On the uplink transmission of extra-large scale massive MIMO systems,” *IEEE Trans. Veh. Technol.*, vol. 69, no. 12, pp. 15 229–15 243, Dec. 2020.
- [39] B. Xu, Z. Wang, H. Xiao, J. Zhang, B. Ai, and D. W. K. Ng, “Low-complexity precoding for extremely large-scale MIMO over non-stationary channels,” *arXiv preprint arXiv:2302.00847*, 2023.
- [40] A. Amiri, M. Angelichinoski, E. De Carvalho, and R. W. Heath, “Extremely large aperture massive MIMO: Low complexity receiver architectures,” in *Proc. IEEE Global Commun. Workshops (GC Wkshps)*, 2018, pp. 1–6.
- [41] J. C. Marinello Filho, G. Brante, R. D. Souza, and T. Abrão, “Exploring the non-overlapping visibility regions in XL-MIMO random access and scheduling,” *IEEE Trans. Wireless Commun.*, vol. 21, no. 8, pp. 6597–6610, Aug. 2022.
- [42] O. S. Nishimura, J. C. Marinello, and T. Abrão, “A grant-based random access protocol in extra-large massive MIMO system,” *IEEE Commun. Lett.*, vol. 24, no. 11, pp. 2478–2482, Nov. 2020.
- [43] J. C. Marinello, T. Abrão, A. Amiri, E. De Carvalho, and P. Popovski, “Antenna selection for improving energy efficiency in XL-MIMO systems,” *IEEE Trans. Veh. Tech.*, vol. 69, no. 11, pp. 13 305–13 318, Nov. 2020.
- [44] C. A. Balanis, *Antenna theory: analysis and design*. John Wiley & sons, 2016.
- [45] A. Poon, R. Brodersen, and D. Tse, “Degrees of freedom in multiple-antenna channels: a signal space approach,” *IEEE Trans. Inf. Theory*, vol. 51, no. 2, pp. 523–536, Feb. 2005.
- [46] K. Zhi, C. Pan, H. Ren, K. Wang, M. ElKashlan, M. Di Renzo, R. Schober, H. Vincent Poor, J. Wang, and L. Hanzo, “Two-timescale design for reconfigurable intelligent surface-aided massive MIMO systems with imperfect CSI,” *IEEE Trans. Inf. Theory*, vol. 69, no. 5, pp. 3001–3033, 2023.
- [47] K. Zhi, C. Pan, H. Ren, K. K. Chai, and M. ElKashlan, “Active RIS versus passive RIS: Which is superior with the same power budget?” *IEEE Commun. Lett.*, vol. 26, no. 5, pp. 1150–1154, May 2022.
- [48] M. Cui, L. Dai, R. Schober, and L. Hanzo, “Near-field wideband beamforming for extremely large antenna arrays,” *arXiv preprint arXiv:2109.10054*, 2021.
- [49] T. Brown, P. Kyritsi, and E. De Carvalho, *Practical Guide to MIMO Radio Channel: With MATLAB Examples*. John Wiley & Sons, 2012.
- [50] K. Zhi, C. Pan, H. Ren, and K. Wang, “Power scaling law analysis and phase shift optimization of RIS-aided massive MIMO systems with statistical CSI,” *IEEE Trans. Commun.*, vol. 70, no. 5, pp. 3558–3574, May 2022.
- [51] G. Interdonato, M. Karlsson, E. Björnson, and E. G. Larsson, “Local partial zero-forcing precoding for cell-free massive MIMO,” *IEEE Trans. Wireless Commun.*, vol. 19, no. 7, pp. 4758–4774, Sep. 2020.
- [52] K. Zhi, G. Chen, L. Qiu, X. Liang, and C. Ren, “Analysis and optimization of random cache in multi-antenna HetNets with interference nulling,” in *Proc. IEEE Global Commun. Conf. (Globecom)*, 2019, pp. 1–6.
- [53] L. Chang, W. Li, and W. Zhang, “Computing a near-maximum independent set in linear time by reducing-peeling,” in *Proc. ACM International Conf. Management of Data*, 2017, pp. 1181–1196.
- [54] I. S. Gradshteyn and I. M. Ryzhik, *Table of Integrals, Series, and Products*. Academic Press, 2014.



Kangda Zhi received the B.Eng degree from the School of Communication and Information Engineering, Shanghai University (SHU), Shanghai, China, in 2017, the M.Eng degree from School of Information Science and Technology, University of Science and Technology of China (USTC), Hefei, China, in 2020, and the Ph.D. degree from the School of Electronic Engineering and Computer Science, Queen Mary University of London, U.K., in 2023. His research interests include Reconfigurable Intelligent Surface (RIS), massive MIMO, and near-field communications. He received the Exemplary Reviewer Certificate of the IEEE WIRELESS COMMUNICATIONS LETTERS in 2021 and 2022.



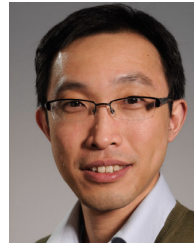
Cunhua Pan received the B.S. and Ph.D. degrees from the School of Information Science and Engineering, Southeast University, Nanjing, China, in 2010 and 2015, respectively. From 2015 to 2016, he was a Research Associate at the University of Kent, U.K. He held a post-doctoral position at Queen Mary University of London, U.K., from 2016 and 2019. From 2019 to 2021, he was a Lecturer in the same university. From 2021, he is a full professor in Southeast University.

His research interests mainly include reconfigurable intelligent surfaces (RIS), intelligent reflection surface (IRS), ultra-reliable low latency communication (URLLC), machine learning, UAV, Internet of Things, and mobile edge computing. He has published over 120 IEEE journal papers. He is currently an Editor of IEEE Transactions on Vehicular Technology, IEEE Wireless Communication Letters, IEEE Communications Letters and IEEE ACCESS. He serves as the guest editor for IEEE Journal on Selected Areas in Communications on the special issue on xURLLC in 6G: Next Generation Ultra-Reliable and Low-Latency Communications. He also serves as a leading guest editor of IEEE Journal of Selected Topics in Signal Processing (JSTSP) Special Issue on Advanced Signal Processing for Reconfigurable Intelligent Surface-aided 6G Networks, leading guest editor of IEEE Vehicular Technology Magazine on the special issue on Backscatter and Reconfigurable Intelligent Surface Empowered Wireless Communications in 6G, leading guest editor of IEEE Open Journal of Vehicular Technology on the special issue of Reconfigurable Intelligent Surface Empowered Wireless Communications in 6G and Beyond, and leading guest editor of IEEE ACCESS Special Issue on Reconfigurable Intelligent Surface Aided Communications for 6G and Beyond. He is Workshop organizer in IEEE ICC 2021 on the topic of Reconfigurable Intelligent Surfaces for Next Generation Wireless Communications (RIS for 6G Networks), and workshop organizer in IEEE Globecom 2021 on the topic of Reconfigurable Intelligent Surfaces for future wireless communications. He is currently the Workshops and Symposia officer for Reconfigurable Intelligent Surfaces Emerging Technology Initiative. He is workshop chair for IEEE WCNC 2024, and TPC co-chair for IEEE ICCT 2022. He serves as a TPC member for numerous conferences, such as ICC and GLOBECOM, and the Student Travel Grant Chair for ICC 2019. He received the IEEE ComSoc Leonard G. Abraham Prize in 2022, IEEE ComSoc Asia-Pacific Outstanding Young Researcher Award, 2022.



Hong Ren received the B.S. degree in electrical engineering from Southwest Jiaotong University, Chengdu, China, in 2011, and the M.S. and Ph.D. degrees in electrical engineering from Southeast University, Nanjing, China, in 2014 and 2018, respectively. From 2016 to 2018, she was a Visiting Student with the School of Electronics and Computer Science, University of Southampton, U.K. From 2018 to 2020, she was a Post-Doctoral Scholar with Queen Mary University of London, U.K. She is currently an associate professor with Southeast

University. Her research interests lie in the areas of communication and signal processing, including ultra-low latency and high reliable communications, Massive MIMO and machine learning.



Kok Keong Chai received the B.Eng. (Hons.), M.Sc., and Ph.D. degrees, in 1998, 1999, and 2007, respectively. He joined the School of Electronic Engineering and Computer Science (EECS), Queen Mary University of London (QMUL), in August 2008. He is currently a Professor in the Internet of Things, the Queen Mary Director of Joint Programme with the Beijing University of Posts and Telecommunications (BUPT), and a Communication Systems Research Group Member of QMUL. He has authored more than 65 technical journals and conference papers in his research areas. His current research interests include sensing and prediction in distributed smart grid networks, smart energy charging schemes, applied blockchain technologies, dynamic resource management, wireless communications, and medium access control (MAC) for M2M communications and networks.



Cheng-Xiang Wang (Fellow, IEEE) received the B.Sc. and M.Eng. degrees in communication and information systems from Shandong University, China, in 1997 and 2000, respectively, and the Ph.D. degree in wireless communications from Aalborg University, Denmark, in 2004.

He was a Research Assistant with the Hamburg University of Technology, Hamburg, Germany, from 2000 to 2001, a Visiting Researcher with Siemens AG Mobile Phones, Munich, Germany, in 2004, and a Research Fellow with the University of Agder, Grimstad, Norway, from 2001 to 2005. He has been with Heriot-Watt University, Edinburgh, U.K., since 2005, where he was promoted to a Professor in 2011. In 2018, he joined Southeast University, Nanjing, China, as a Professor. He is also a part-time Professor with Purple Mountain Laboratories, Nanjing. He has authored 4 books, 3 book chapters, and 520 papers in refereed journals and conference proceedings, including 27 highly cited papers. He has also delivered 24 invited keynote speeches/talks and 16 tutorials in international conferences. His current research interests include wireless channel measurements and modeling, 6G wireless communication networks, and electromagnetic information theory.

Dr. Wang is a Member of the Academia Europaea (The Academy of Europe), a Member of the European Academy of Sciences and Arts (EASA), a Fellow of the Royal Society of Edinburgh (FRSE), IEEE, IET and China Institute of Communications (CIC), an IEEE Communications Society Distinguished Lecturer in 2019 and 2020, a Highly-Cited Researcher recognized by Clarivate Analytics in 2017-2020. He is currently an Executive Editorial Committee Member of the IEEE TRANSACTIONS ON WIRELESS COMMUNICATIONS. He has served as an Editor for over ten international journals, including the IEEE TRANSACTIONS ON WIRELESS COMMUNICATIONS, from 2007 to 2009, the IEEE TRANSACTIONS ON VEHICULAR TECHNOLOGY, from 2011 to 2017, and the IEEE TRANSACTIONS ON COMMUNICATIONS, from 2015 to 2017. He was a Guest Editor of the IEEE JOURNAL ON SELECTED AREAS IN COMMUNICATIONS, Special Issue on Vehicular Communications and Networks (Lead Guest Editor), Special Issue on Spectrum and Energy Efficient Design of Wireless Communication Networks, and Special Issue on Airborne Communication Networks. He was also a Guest Editor for the IEEE TRANSACTIONS ON BIG DATA, Special Issue on Wireless Big Data, and is a Guest Editor for the IEEE TRANSACTIONS ON COGNITIVE COMMUNICATIONS AND NETWORKING, Special Issue on Intelligent Resource Management for 5G and Beyond. He has served as a TPC Member, a TPC Chair, and a General Chair for more than 30 international conferences. He received 15 Best Paper Awards from IEEE GLOBECOM 2010, IEEE ICCT 2011, ITST 2012, IEEE VTC 2013 Spring, IWCMC 2015, IWCMC 2016, IEEE/CIC ICC 2016, WPMC 2016, WOCC 2019, IWCMC 2020, WCSP 2020, CSPS2021, WCSP 2021, and IEEE/CIC ICC 2022.



Robert Schober (S'98, M'01, SM'08, F'10) received the Diplom (Univ.) and the Ph.D. degrees in electrical engineering from Friedrich-Alexander University of Erlangen-Nuremberg (FAU), Germany, in 1997 and 2000, respectively. From 2002 to 2011, he was a Professor and Canada Research Chair at the University of British Columbia (UBC), Vancouver, Canada. Since January 2012 he is an Alexander von Humboldt Professor and the Chair for Digital Communication at FAU. His research interests fall into the broad areas of Communication Theory,

Wireless and Molecular Communications, and Statistical Signal Processing.

Robert received several awards for his work including the 2002 Heinz Maier Leibnitz Award of the German Science Foundation (DFG), the 2004 Innovations Award of the Vodafone Foundation for Research in Mobile Communications, a 2006 UBC Killam Research Prize, a 2007 Wilhelm Friedrich Bessel Research Award of the Alexander von Humboldt Foundation, the 2008 Charles McDowell Award for Excellence in Research from UBC, a 2011 Alexander von Humboldt Professorship, a 2012 NSERC E.W.R. Stacie Fellowship, a 2017 Wireless Communications Recognition Award by the IEEE Wireless Communications Technical Committee, and the 2022 IEEE Vehicular Technology Society Stuart F. Meyer Memorial Award. Furthermore, he received numerous Best Paper Awards for his work including the 2022 ComSoc Stephen O. Rice Prize and the 2023 ComSoc Leonard G. Abraham Prize. Since 2017, he has been listed as a Highly Cited Researcher by the Web of Science. Robert is a Fellow of the Canadian Academy of Engineering, a Fellow of the Engineering Institute of Canada, and a Member of the German National Academy of Science and Engineering.

He served as Editor-in-Chief of the IEEE Transactions on Communications, VP Publications of the IEEE Communication Society (ComSoc), ComSoc Member at Large, and ComSoc Treasurer. Currently, he serves as Senior Editor of the Proceedings of the IEEE and as ComSoc President-Elect.



Xiao-Hu You received his Master and Ph.D. Degrees from Southeast University, Nanjing, China, in Electrical Engineering in 1985 and 1988, respectively. Since 1990, he has been working with National Mobile Communications Research Laboratory at Southeast University, where he is currently professor and director of the Lab. He has contributed over 300 IEEE journal papers and 3 books in the areas of wireless communications. From 1999 to 2002, he was the Principal Expert of China C3G Project. From 2001-2006, he was the Principal Expert of

China National 863 Beyond 3G FuTURE Project. From 2013 to 2019, he was the Principal Investigator of China National 863 5G Project. His current research interests include wireless networks, advanced signal processing and its applications.

Dr. You was selected as IEEE Fellow in 2011. He served as the General Chair for IEEE Wireless Communications and Networking Conference (WCNC) 2013, IEEE Vehicular Technology Conference (VTC) 2016 Spring, and IEEE International Conference on Communications (ICC) 2019.